https://doi.org/10.5194/gmd-2024-213
Preprint. Discussion started: 13 December 2024

Geoscientific Model Development
Discussions
Open Access

Impacts of CICE sea ice model and ERA atmosphere on an Antarctic MetROMS ocean model, MetROMS-UHel-v1.0

Cecilia Äijälä[1], Yafei Nie[2], Lucía Gutiérrez-Loza[3], Chiara De Falco[3], Siv Kari Lauvset[3], Bin Cheng[4], David A. Bailey[5], and Petteri Uotila[1]

[1]University of Helsinki, Institute for Atmospheric and Earth System Research / Physics, Helsinki, Finland
[2]School of Atmospheric Sciences, Sun Yat-Sen University, and Southern Marine Science and Engineering Guangdong Laboratory (Zhuhai), Zhuhai, China
[3]NORCE Norwegian Research Centre, Bjerknes Centre for Climate Research, Norway
[4]Finnish Meteorological Institute. Polar meteorology and climatology research group, Helsinki, Finland
[5]NSF National Center for Atmospheric Research, Boulder, Colorado, USA

Correspondence: Cecilia Äijälä (cecilia.aijala@helsinki.fi)

Abstract.

In recent years, the Antarctic sea ice has experienced major changes, which are neither well understood nor adequately reproduced by earth system models. To support model development with an aim to improve Antarctic sea ice and upper ocean predictions, the impacts of updating the sea ice model and the atmospheric forcing are investigated. In the new MetROMS-UHel-v1.0 (henceforth MetROMS-UHel) ocean-sea ice model, the sea ice component has been updated from CICE5 to CICE6, and the forcing has been updated from ERA-Interim to ERA5 reanalyses. Both CICE sea ice models were coupled with the regional ROMS ocean model. We find that the update of CICE and ERA reduced the negative bias of the sea ice area in summer. However, the sea ice volume decreases after the CICE update but increase when the atmospheric forcing is updated. As a net result after both updates, the modelled sea ice becomes thinner and more deformed, particularly near the coast. The ROMS ocean model usually yielded a deeper ocean mix layer compared to observations. Using ERA5, the situation was slightly improved. The update from CICE5 to CICE6 resulted in a fresher coastal ocean due to a smaller salt flux from sea ice to the ocean. In the ice shelf cavities, the modelled melt rates are underestimated compared with observations, which could be attributed to missing tides and inadequate model resolution. These identified sea ice and oceanic changes vary seasonally and regionally. By determining sea ice and oceanic changes after the model and forcing updates, and evaluating them against observations, this study informs modellers on improvements and aspects requiring attention with potential model adjustments.

1 Introduction

The Southern Ocean is a key component in the global climate system, influencing the global ocean circulation and climate. In particular, sea ice plays a crucial role by regulating heat exchanges between ocean and atmosphere, controlling salt fluxes and freshwater distribution, and significantly impacting the uptake and storage of CO_2 (Rintoul, 2018). In recent years, this region has experienced significant changes. Following a decades-long gradual overall increase, Antarctic sea ice is experiencing a rapid decrease after reaching a record high extent in 2014 (Parkinson, 2019). The minimum summer sea ice extent in 2022, 2023, and 2024 are the three lowest measured in 46 years of satellite records (Purich and Doddridge, 2023; Gilbert and Holmes, 2024; NSIDC, 2024). Furthermore, the winter sea ice maximum of 2023 was a record low (Purich and Doddridge, 2023; Gilbert and Holmes, 2024). Studies have shown an increased variance in Antarctic sea ice cover and a changing response to atmospheric forcing (Hobbs et al., 2024). Furthermore, the sea ice decline has been linked to ocean warming, which has been identified as the underlying cause of shifts in the sea ice regime (Purich and Doddridge, 2023) .

The physical processes behind the recent observed changes are not yet fully understood, and further research is needed. However, studying a dynamic and remote environment, such as the Southern Ocean, is challenging and expensive. In situ observations in the Southern Ocean are sparse and time series short, especially for subsurface ocean measurements and in the sea ice zone, and they are biased towards summer water conditions (Charrassin et al., 2008). Most common measurement systems face technical and logistical challenges in the Antarctic ice covered areas. Surface moorings are hard to deploy due to the high possibility of ice related damage, and floats cannot always resurface to transmit data reliably (Rintoul et al., 2014). Satellite sensors have become indispensable in climate system observations, however, they cannot observe below sea ice and the persistent cloud cover limits their utility at high latitudes. Despite increasing efforts, the Antarctic Ocean below the sea ice and ice shelves remains among the least observed systems (Rintoul et al., 2014). Therefore, accurate modelling of this area is particularly important.

Modelling Antarctic sea ice is also challenging. Its northern boundary is exposed to the Southern Ocean, in a highly dynamic environment, where it is subjected to strong winds, waves and currents. The sea ice properties can vary greatly with ice floes of varying thickness, broken by cracks and leads, and usually covered in snow (Worby et al., 2008). It extends to lower latitudes if compared to its Arctic counterpart and has a higher seasonality, and its thickness is limited by the relatively warm Circumpolar Deep Waters (CDW) (Maksym et al., 2015). Understanding how the different processes affecting the sea ice work in models, and what shortcomings they have, is critical. Model development is continuously ongoing, and new versions of the different components need to be implemented in the models that use them. With better models, we could reduce model uncertainty and potentially improve future projections of the sea ice and the ocean.

This paper presents the circumpolar Antarctic coupled ocean–sea ice model MetROMS-UHel, an updated version of the coupled model, MetROMS-Iceshelf. MetROMS-Iceshelf has been used for studies on ice shelves, the effect of increased basal melt rate on the Antarctic Slope Current, and the transport of sea ice at the coast (Naughten et al., 2018b; Huneke et al., 2023). However, model development and advances in reanalysis products providing higher resolution and near present forcing are both expected to have important implications in the model outputs (Barthélemy et al., 2018). Here, a new implementation of the model, including updates in the sea ice component and atmospheric forcing, is presented. Four simulations with different atmospheric forcing and sea ice module combinations are used to evaluate the impact of such updates on sea ice variables, ice shelf characteristics, and oceanic components. An overview of the model is presented in Sect. 2, while the experimental design is described in Sect. 3. The results are presented and discussed in Sect. 4.

2 Model description

MetROMS-UHel is an updated version of the coupled ocean/sea ice/ice shelf model MetROMS-Iceshelf (Naughten et al., 2017, 2018b). In this new version, the sea ice component has been updated with a newer version (see Sect. 2.1). Furthermore, the atmospheric forcing ERA-Interim (ERAI) (Dee et al., 2011) has been substituted with the latest ECMWF (European Centre for Medium-Range Weather Forecasts) reanalysis version, ERA5 (Hersbach et al., 2017).

2.1 Model overview

MetROMS-Iceshelf and MetROMS-UHel consist of the free-surface, terrain-following Regional Ocean Modelling System (ROMS) (Shchepetkin and McWilliams, 2005) and the dynamic-thermodynamic sea ice model CICE (Community Ice CodE) (Hunke et al., 2015, 2022) coupled with the Model Coupling Toolkit (MCT 2.11) (Larson et al., 2005; Jacob et al., 2005). The ocean physical component for both model versions, MetROMS-Iceshelf and MetROMS-UHel, is the same. They use the development Version 3.7 of the Rutgers ROMS code with ice shelf thermodynamics (Galton-Fenzi et al., 2012). The ocean setup for both models has a baroclinic timestep of 5 min, with 30 barotropic timesteps for each baroclinic timestep.

The coupled MetROMS models use different versions of CICE, specifically, MetROMS-Iceshelf uses CICE 5.1.2 (Hunke et al., 2015) while MetROMS-UHel uses CICE 6.3.1 (Hunke et al., 2022). CICE has been completely reworked between versions 5 and 6, with major restructuring and refactoring of the code, updated physics parametrization and bug fixes. CICE6 has been shown to improve the results of Arctic sea ice compared to CICE5 and CICE4 in the standalone mode (Wang et al., 2020b). The model setup and parameters used for CICE in both models have been kept as similar as possible, using mostly CICE default values. Both versions use the elastic-viscous-plastic dynamics (Hunke and Dukowicz, 2003; Bouillon et al., 2013). For advection, the incremental remapping scheme for sea ice by Lipscomb and Hunke (2004) is employed. For ice strength, the energetics-based approach of Rothrock (1975) is used, with ridging participation and redistribution functions by Lipscomb et al. (2007). Thermodynamics are handled by a mushy-layer thermodynamics scheme (Turner et al., 2013) with a level-pond parametrization (Hunke et al., 2013) with Stefan refreezing. We use the Delta–Eddington radiation scheme (Briegleb et al., 2007; Holland et al., 2012), which calculates apparent optical properties, like albedo, from inherent optical properties. Both models use seven vertical ice layers, one snow layer and five ice thickness categories.

The original coupling was implemented by the Norwegian Meteorological Institute (Debernard et al., 2017), and described in Naughten et al. (2017). The updated coupling of CICE6 in MetROMS-UHel was implemented as part of this work, following the same principles of the original coupling. ROMS and CICE run on separate processors and communicate through the MCT coupler. The models have the same resolution (see Sect. 2.2), but ROMS uses an Arakawa C-grid while CICE uses an Arakawa B-grid (Arakawa and Lamb, 1977). Even though the position of the variables differs between these grids, both model components have the tracers at the cell centre, which is used for the coupling, with variables interpolated there as needed. The variables passed from CICE to ROMS are: sea ice concentration, ice–ocean stress vectors, heat, salt and freshwater fluxes, and shortwave radiation coming through the ice. The variables passed from ROMS to CICE are: sea surface temperature, sea surface salinity, ocean velocity averaged over the top 5 m, sea surface height, and the freeze–melt potential, which is the energy flux (in W m^{-2}) associated with the temperature difference from the freezing point. The coupling timestep for both models is 30 min, the same as the thermodynamic timestep for CICE.

2.2 Domain

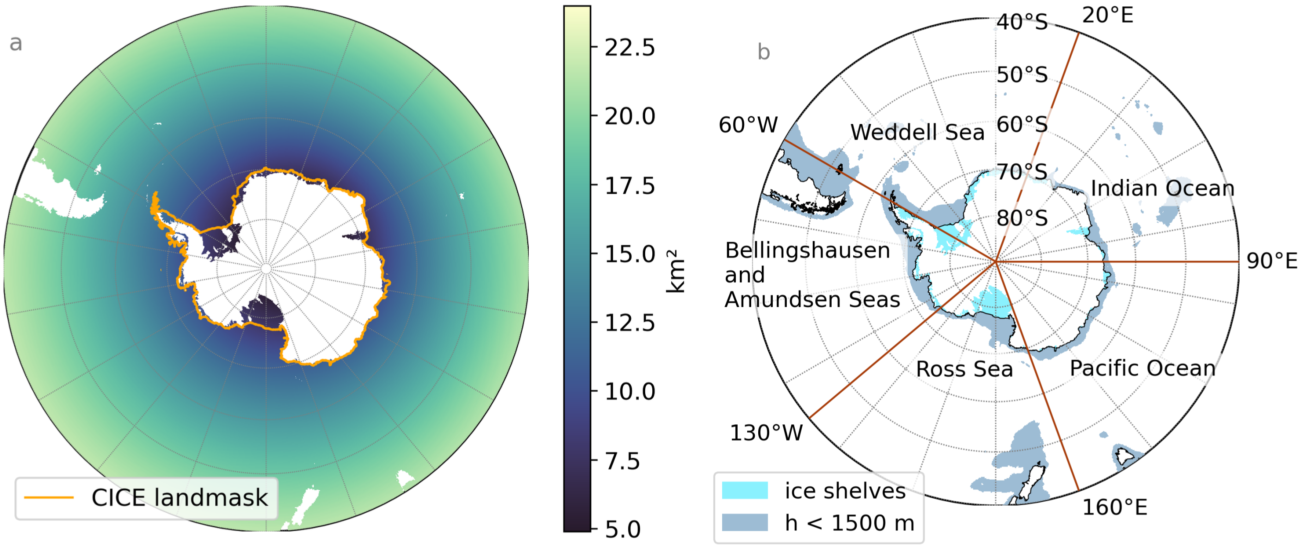

Figure 1. (a) Horizontal resolution of the domain in km^2 (from 40° S). The white area shows the ROMS land mask, and the orange line shows the edge of the CICE land mask around Antarctica. The area between these land masks contains the ice shelves that are included in ROMS, but not in CICE. (b) Map of the five Antarctic sectors used in the analysis. The light blue shading shows the ice shelf cavities and the darker blue indicates areas with depths up to 1500 m, marking the continental shelves.

MetROMS-UHel and MetROMS-Iceshelf use the same grid as in Naughten et al. (2017, 2018b). The grid is a circumpolar Antarctic quarter-degree grid scaled by cosine of latitude and with a relocated South Pole. The northern boundary is at 30° S and in the south the model extends into the ice shelf cavities. The ice shelf draft is static and the bathymetry, ice shelf draft and land/sea mask are calculated from the RTopo-1.05 dataset (Timmermann et al., 2010) using a three-step smoothing procedure described in Naughten et al. (2018b) to ensure stability at the terrain-following coordinates.

The resulting Cartesian resolution of the grid cells is 8–10 km on the shelf and 15–20 km at the Antarctic Circumpolar Current (ACC, around 50° S). At the southernmost grounding lines of the Filchner-Ronne, Amery, and Ross ice sheets the grid resolution is 5 km or even finer (Fig. 1a). The ocean model has 31 terrain-following vertical levels. This sigma coordinate results in a varying vertical resolution, being 1–3 m at the surface, and 200–300 m in the deep interior ocean. In the ice shelf cavities, the vertical resolution can often be less than 1 m.

3 Experiment design

Table 1. Description of the four ocean–sea ice model simulations analysed in this study.

Experiment name	Model	CICE version	Atmospheric forcing	Modelling time
C5EI	MetROMS-Iceshelf	CICE 5.1.2	ERAI	January 1992–August 2019
C5E5	MetROMS-Iceshelf	CICE 5.1.2	ERA5	January 1992–April 2023
C6EI	MetROMS-UHel	CICE 6.3.1	ERAI	January 1992–August 2019
C6E5	MetROMS-UHel	CICE 6.3.1	ERA5	January 1992–April 2023

Four experiments with different atmospheric forcing and sea ice module combinations are used (see Table 1) to evaluate the performance of the new MetROMS-UHel in comparison to MetROMS-Iceshelf. These simulations allow us to assess the impacts of the updated sea ice model and those attributed to the atmospheric forcing on the model outputs. Two of the simulations, C5CI and C5C5, use the MetROMS-Iceshelf setup where the old sea ice component CICE5 is used, but each simulation is forced with a different atmospheric reanalysis (ERAI and ERA5, respectively). Similarly, the simulations C6EI and C6E5 using the MetROMS-UHel setup with the updated sea ice component CICE6 are forced with ERAI and ERA5, respectively. All simulations start in January 1992 and run until the end of the forcing data (August 2019 for ERAI and April 2023 for ERA5). The initial conditions, spinup, and forcing are described in the two following sections.

3.1 Initial conditions and spinup

The ROMS ocean initial conditions for temperature and salinity are from the ECCO2 cube 92 reanalyses (Menemenlis et al., 2008; Wunsch et al., 2009), and January 1992 is used. Temperature and salinity have been extrapolated to the ice shelf cavities using the nearest neighbour method. Initial velocities and sea surface height are set to 0.

The initial conditions for the sea ice in CICE are created using an ice mask which sets ice where the NOAA/NSIDC Climate Data Record of Passive Microwave Sea Ice Concentration Version 2 (Meier et al., 2013) shows concentrations greater than 15 %. In these areas, the model initializes the ice to be 1 m thick with 100 % concentration and 0.2 m of snow on top of the sea ice.

All experiments are initialized with a short spinup. The model is run for 5 years with the forcing for year 1992 before switching to yearly forcing. The spinup is not enough for the ocean model to reach an equilibrium state. However, the spinup is enough for the sea ice and upper ocean to reach equilibrium and for the total kinetic energy of the regional model to even out. Therefore, for the analysis of the surface and continental shelves, we argue that a full spinup is not worth the needed computational power. The basal melt rate of the ice shelves takes until year 1996 to even out (8 years) and basal melt is therefore analyzed for the period 1996–2018 (Sect. 4.3). The deep ocean does not reach equilibrium and some model drift can be seen in the interior ocean, for example, in ACC transport (not shown). Similar decreasing trends of the ACC are found in the MetROMS-Iceshelf runs by Naughten et al. (2018b).

https://doi.org/10.5194/gmd-2024-213
Preprint. Discussion started: 13 December 2024

3.2 Forcing

We run the models with atmospheric forcing from two different reanalyses from ECMWF, ERAI and the newer ERA5. ERA5 is a considerable upgrade from ERAI with a finer horizontal resolution of 31 km compared to the ERAI 80 km, and development in model physics, numerics, and data assimilation (Hersbach and de Rosnay, 2018). The atmospheric reanalyses are interpolated to the model grid, and the ERA5 hourly data are interpolated to the same temporal resolution that is used for ERAI. We use 6-hourly near-surface temperature, pressure, humidity, winds, and total cloud cover. Additionally, we use 12-hourly rain, snow, and evaporation. The 6-hourly data are linearly interpolated in the model for each timestep (5 min for ROMS and 30 min for CICE), and the 12-hourly data are applied at a constant rate with a step change every 12 h. Freshwater flux from iceberg melt is also added using a monthly averaged 100-year climatology from Martin and Adcroft (2010) as in Naughten et al. (2018b).

We apply the same salinity restoration scheme to ROMS in all the model runs, as previously used in MetROMS-Iceshelf by Naughten et al. (2018b). The World Ocean Atlas 2013 (WOA13) monthly climatology by Zweng et al. (2013) is linearly interpolated for each model timestep and repeated annually. The salinity restoration is applied on a 30-day timescale to the uppermost layer. Following Naughten et al. (2018b), the restoration is not applied on the Antarctic continental shelf (i.e., areas south of 60° S where the depth is less than 1500 m) nor in the ice shelf cavities (see Fig. 1b) to reduce the excessive freshening of Antarctic Bottom Water (ABW).

For the northern boundaries in ROMS, we use monthly ECCO2 reanalysis temperature, salinity, and horizontal velocity, while zonal velocity is clamped to 0, such that there is flow through the border but not along it. The numerical methods used to apply boundary conditions are the Radiation-Nudging scheme (Marchesiello et al., 2001) for baroclinic meridional velocity, temperature, and salinity. This scheme combines a radiation condition with nudging to external data. The radiation condition, combined with a weak nudging, minimizes the reflection of internal information propagating out of the domain and avoids drifting. A stronger nudging is applied to incoming data. The Flather scheme (Flather, 1976) is used for barotropic meridional velocity, where differences in modelled and boundary sea surface height are used to tune the normal velocity. This method avoids over-specification due to simple clamping (Mason et al., 2010) but still allows mass-balance conservation (Carter and Merrifield, 2007). The Chapman scheme (Chapman, 1985) for sea surface height, which is often used in combination with the Flather scheme, is derived from the linearized gravity wave equation and designed to minimize the reflection of model gravity waves propagating outwards (Mason et al., 2010). For sea surface height, we use the AVISO climatology (AVISO, 2011). To make the transition into the domain, we apply a constant topography in the y direction to the 15 northernmost cells, which corresponds to around 3° in latitude. CICE does not require northern boundary conditions, as the sea ice edge does not come close to the northern boundary of the model

https://doi.org/10.5194/gmd-2024-213
Preprint. Discussion started: 13 December 2024

4 Results and Discussion

4.1 Sea Ice

4.1.1 Sea Ice Concentration and Area

The modelled sea ice concentration is compared with satellite observations from NOAA/NSIDC Climate Data Record of Passive Microwave Sea Ice Concentration, Version 4 (Meier et al., 2021), referred to as NSIDC CDR hereafter. The ice edge is defined as the point where sea ice concentration reaches 15 %. It's important to note that sea ice concentrations below this threshold are uncertain in satellite measurements (Zwally et al., 1983), which should be considered when interpreting the results. In general, all simulations underestimate the sea ice concentration compared to NSIDC CDR (Fig. 2), but updating the model and atmospheric forcing increases the concentration (Fig. A1). However, some large-scale patterns are observed, including both underestimation and overestimation of the sea ice concentration, that are consistent throughout all model runs.

During the summer (JFM), the largest underestimations of the sea ice concentration are observed in the western region of the Weddell Sea sector and close to the coast and ice edge in the Indian Ocean, Pacific Ocean, and the Bellinghausen and Amundsen Seas (BellAm hereafter) sectors (Fig. 2e, i, m, q). Sea ice concentration is overestimated in the eastern Weddell Sea and the Ross Sea sectors, primarily north of the ice edge (black line in Fig. 2), except for C6E5, where the majority of the Ross Sea sector is also overestimated (Fig. 2q). Updating the sea ice model from CICE5 to CICE6 decreases the sea ice concentration close to the coast, especially in the Indian Ocean sector (Fig. A1i), while both the change from ERAI to ERA5 and from CICE5 to CICE6 increase the concentration in the Ross Sea, BellAm, and Weddell Sea sectors (Fig. A1m), which decreases the underestimation compared to the satellite measurements seen in these sectors south of the ice edge.

In autumn (AMJ), the sea ice concentration is mostly underestimated in the models compared to NSIDC CDR satellite measurements (Fig. 2f, j, n, r), but not as much as in summer. However, closer to the coast where sea ice concentrations are close to 100 %, the models perform well, particularly south of 70° S in the Weddell Sea and Ross Sea sectors. The models overestimate the sea ice close to the ice edge in the Antarctic Peninsula at the border of the BellAm and Weddell Sea sectors and in some coastal areas.

The differences between the modelled and the observed sea ice concentration during winter (JAS) show similar spatial patterns to those observed during the autumn (AMJ) (Fig. 2g, k, o, s). However, along the ice edge, an increased overestimation is observed in the Weddell Sea sector, while large underestimations occur in the other sectors. The differences in sea ice concentration among the different model runs is largest close to the ice edge, especially in the BellAm and Weddell Sea sectors, where the largest concentrations can be found from C6E5 (Fig. A1o).

The spatial pattern of the differences in the concentration between the model runs and NSIDC CDR is more variable in spring (OND) than in the other seasons, with both underestimation and overestimation happening in the entire domain (Fig. 2h, l, p, t). Nevertheless, the observed patterns are consistent throughout the model runs. The overestimation happens mostly close to the ice edge and large parts of the Indian Ocean sector, while underestimation occurs largely in coastal areas and the Weddell and Ross Seas. On the one hand, changing the atmospheric forcing from ERAI to ERA5 tends to increase the concentration

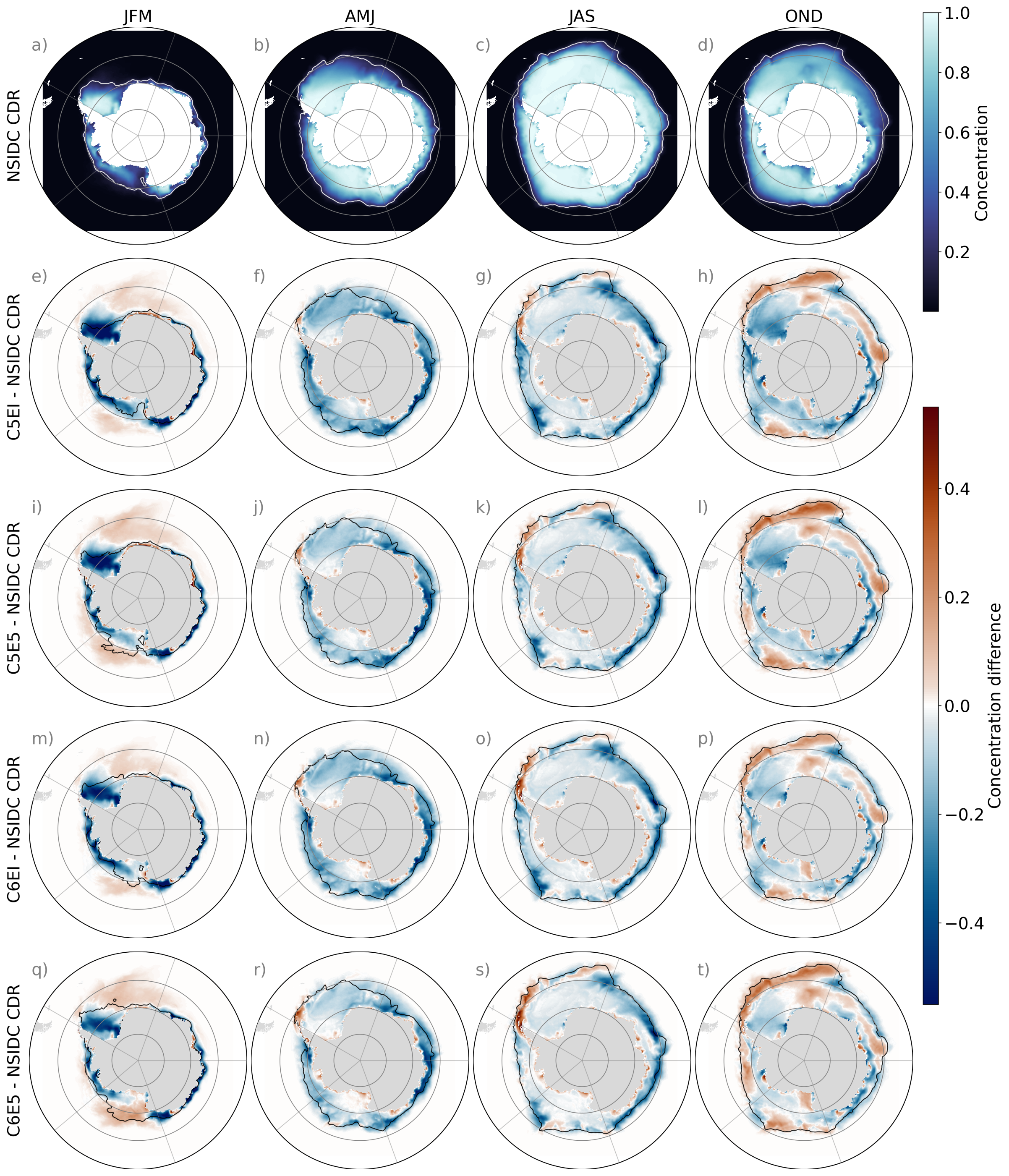

Figure 2. (a–d) Seasonal mean sea ice concentration over the period 1992–2018 from NSIDC CDR and (e–t) concentration differences between NSIDC CDR and the different model runs (C5EI, C5E5, C6EI, C6E5). The white (black) line shows the sea ice edge of the observations (model). The sea ice edge is defined using a 15 % sea ice concentration threshold.

https://doi.org/10.5194/gmd-2024-213
Preprint. Discussion started: 13 December 2024

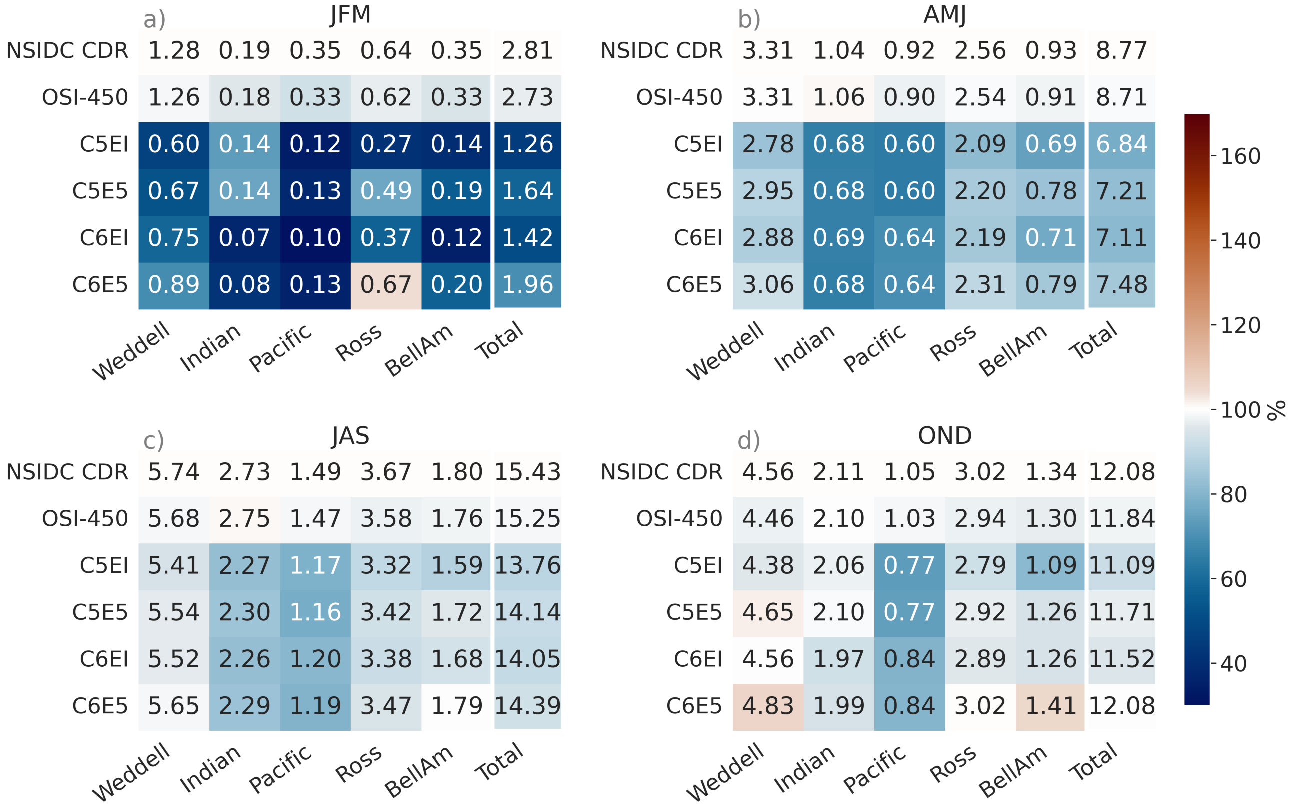

a) JFM

	Weddell	Indian	Pacific	Ross	BellAm	Total
NSIDC CDR	1.28	0.19	0.35	0.64	0.35	2.81
OSI-450	1.26	0.18	0.33	0.62	0.33	2.73
C5EI	0.60	0.14	0.12	0.27	0.14	1.26
C5E5	0.67	0.14	0.13	0.49	0.19	1.64
C6EI	0.75	0.07	0.10	0.37	0.12	1.42
C6E5	0.89	0.08	0.13	0.67	0.20	1.96

b) AMJ

	Weddell	Indian	Pacific	Ross	BellAm	Total
NSIDC CDR	3.31	1.04	0.92	2.56	0.93	8.77
OSI-450	3.31	1.06	0.90	2.54	0.91	8.71
C5EI	2.78	0.68	0.60	2.09	0.69	6.84
C5E5	2.95	0.68	0.60	2.20	0.78	7.21
C6EI	2.88	0.69	0.64	2.19	0.71	7.11
C6E5	3.06	0.68	0.64	2.31	0.79	7.48

c) JAS

	Weddell	Indian	Pacific	Ross	BellAm	Total
NSIDC CDR	5.74	2.73	1.49	3.67	1.80	15.43
OSI-450	5.68	2.75	1.47	3.58	1.76	15.25
C5EI	5.41	2.27	1.17	3.32	1.59	13.76
C5E5	5.54	2.30	1.16	3.42	1.72	14.14
C6EI	5.52	2.26	1.20	3.38	1.68	14.05
C6E5	5.65	2.29	1.19	3.47	1.79	14.39

d) OND

	Weddell	Indian	Pacific	Ross	BellAm	Total
NSIDC CDR	4.56	2.11	1.05	3.02	1.34	12.08
OSI-450	4.46	2.10	1.03	2.94	1.30	11.84
C5EI	4.38	2.06	0.77	2.79	1.09	11.09
C5E5	4.65	2.10	0.77	2.92	1.26	11.71
C6EI	4.56	1.97	0.84	2.89	1.26	11.52
C6E5	4.83	1.99	0.84	3.02	1.41	12.08

Figure 3. Seasonal means of sea ice area for the period 1992–2018 in the different Antarctic sectors (Fig. 1b). The first two rows are satellite observations from NSIDC CDR and OSI-450. The last four rows are the different model runs (C5EI, C5E5, C6EI, C6E5), The numbers are the area of sea ice [10^6 km^2], and the colour is the fraction of the area compared to the NSIDC CDR *([model area]/[NSIDC CDR area])*.

in the Weddell Sea, Ross Sea, and BellAm sectors (Fig. A1h). On the other hand, updating the sea ice model from CICE5 to CICE6 decreases the concentration close to the ice edge in the Weddell Sea, Indian Ocean, and Ross Sea sectors, and at most of the coastline, but increases the concentration otherwise (Fig. A1l).

The modelled sea ice area is compared to NSIDC CDR and the Global Sea Ice Concentration Climate Data Record, OSI-450 (OSI SAF, 2022). The area is calculated from the concentration for both the satellite products and the model simulations as the sum of the sea ice concentration (>15 %) multiplied by the cell area. The four model runs have, in most cases, a smaller total area compared to the satellite observations (Fig. 3). Overall, the sea ice area from C6E5 is the closest to the NSIDC CDR satellite measurements during all seasons, while C5EI has the largest differences. The C5E5 run is the second closest to the observations, which implies that the change from ERAI to ERA5 has generally a stronger effect than the change from CICE5 to CICE6. When comparing the satellite products, OSI-450 has a slightly lower total area than NSIDC CDR. Nevertheless, the

OSI-450 total area is still consistently larger than the model runs in all seasons, except spring (OND). Throughout the year, the largest underestimations happen in the Pacific and Indian Ocean sectors.

During the summer (JFM), every model run underestimates the area compared to NSIDC CDR and OSI-450 in all sectors, except for C6E5 in the Ross Sea (Fig. 3a). Underestimated summer sea ice is a common bias in both standalone ocean models and coupled models (Naughten et al., 2018b; Goosse et al., 2023; Roach et al., 2020; Schroeter and Sandery, 2022). Furthermore, differences between the modelled and the observed total sea ice area are largest during the summer (JFM), as is the variability between the different model runs. Differences in the modelled sea ice areas can be seen especially in the Weddell Sea and Ross Sea sectors where C6E5 is closest to the satellite measurements, and in the Indian Ocean sector where the ice-covered area drops by half when changing from CICE5 to CICE6, placing C6EI and C6E5 further away from the satellite reference values.

Through autumn (AMJ) and winter (JAS), the differences between satellite and modelled sea ice areas are smaller than in the other seasons. Overall, model runs have smaller sea ice areas than the satellite observations, being C6E5 the closest to the satellite measurements in all sectors (Fig. 3b, c).

During spring (OND) models show more variability with both overestimation and underestimation of the sea ice area compared to the observations in the different sectors and model runs (Fig. 3d). The Pacific sector consistently shows underestimations in all model runs during spring (OND), while clear overestimations are observed in the Weddell Sea in the models forced with ERA5 (i.e. C5E5 and C6E5), as well as in the BellAm sector from the C6E5 simulation. Nevertheless, the overall differences between modelled sea ice areas and NSDIC CDR are the smallest during this season as underestimations and overestimations cancel each other out (see Fig. 2), except in the Pacific sector.

Additionally, the temporal changes of the minimum and maximum sea ice area throughout the period 1992–2022 are analysed. The model outputs from February (minimum) and September (maximum) sea ice area are compared to NSIDC CDR and the Sea Ice Index, Version 3 (Fetterer et al., 2021) (Fig. 4). The NSIDC CDR sea ice concentration is calculated as the maximum of the NASA Bootstrap (Comiso and Nishio, 2008) and the NASA Team algorithms (Cavalieri et al., 1997), while the Sea Ice Index uses only the NASA Team algorithm. From these, the NASA Team algorithm tends to get lower concentration values in the pack ice than the bootstrap method (Screen, 2011), and thus have a lower area. For both months, we see that all model runs follow the observed year-to-year variation relatively well (Fig. 4). For example, the decline in the sea ice area around 2015 and its recovery until 2020, with a decline again in 2021 and 2022 can be seen, even though the degree of recovery is smaller in the models than in the observations. In February, both the Sea Ice Index and the NSIDC CDR datasets show larger sea ice areas than the model runs, with the Sea Ice Index being slightly lower than NSIDC CDR (Fig. 4a). The simulations forced with ERA5 (C5E5 and C6E5) show, most of the time, larger values of the minimum sea ice area than those forced with ERAI (C5EI and C6EI). Such a pattern is consistent with the seasonal sea ice area means in Fig. 3. The differences between experiments using CICE5 and CICE6 are not systematic and vary from year to year. In September, modelled sea ice areas are between the Sea Ice Index and the NSIDC CDR, with NSIDC CDR having larger values than the Sea Ice Index (Fig. 4b). Out of the four model runs, the C5E6 run shows the highest sea ice area, closer to NSIDC CDR, while C5EI gives lower values similar to those from the Sea Ice Index.

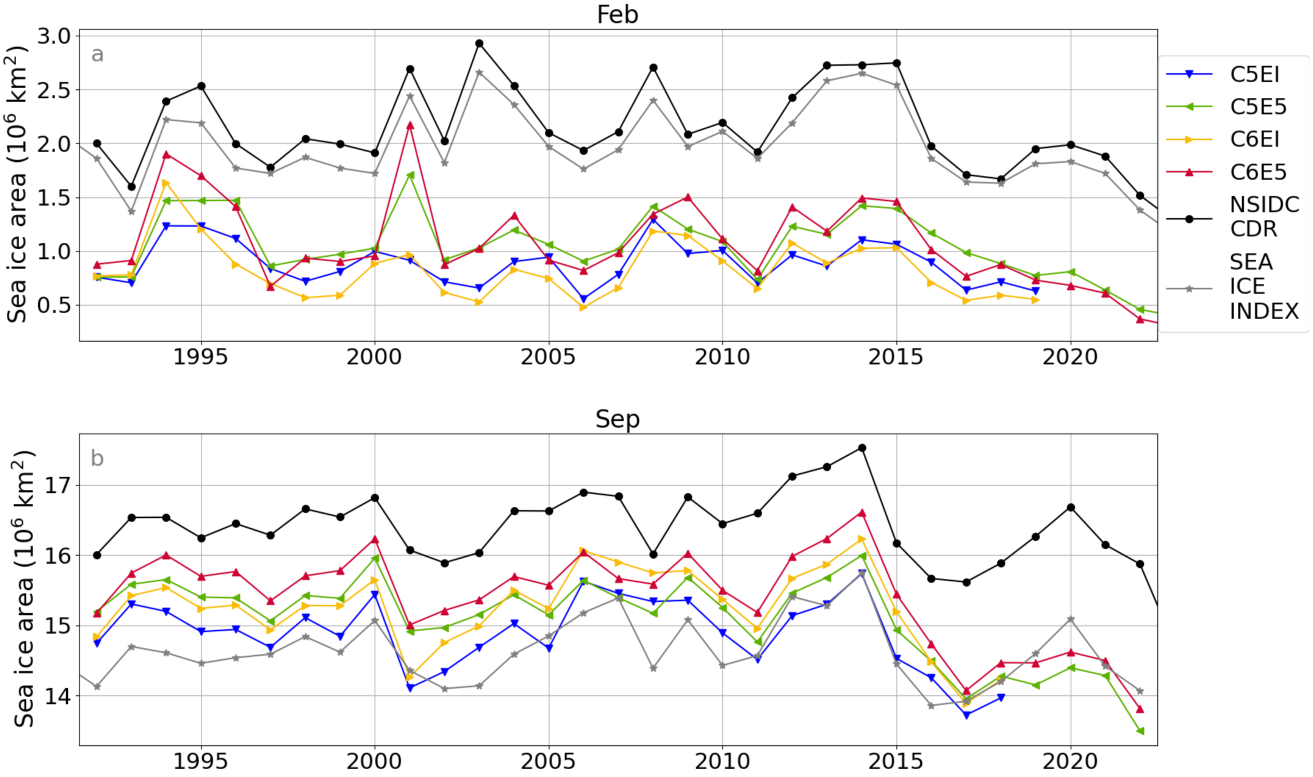

Figure 4. Timeseries over 1992–2022 of (a) February and (b) September monthly average sea ice area [10^6 km^2] for the four different model runs (blue, green, yellow, red) and Sea Ice Index (grey) and NSIDC CDR sea ice concentration (black).

Overall, the results for concentration and area are consistent with each other. Updates in the atmospheric forcing from ERAI to ERA5, and the sea ice model from CICE5 to CICE6, are shown to reduce the underestimation of both sea ice concentration and area, relative to satellite observations (e.g., NSIDC CDR). The change in atmospheric forcing has, on average, a larger effect on the sea ice area than the sea ice model. The underestimation of the sea ice is largest in the summer (JFM). For models using ERAI forcing, low summer sea ice has been attributed to a bias of low cloud cover in ERAI (Naud et al., 2014) that leads to excessive sea ice melt (Naughten et al., 2018b). ERA5 has also been shown to have a similar bias (Wang et al., 2020a), but biases in cloud cover are smaller in ERA5 than in ERAI (Wu et al., 2023). The atmospheric forcing has also been shown to have a warm bias in surface temperature in some areas. For example, in the Weddell Sea, both atmospheric reanalyses are shown to have a warm surface bias compared to buoy measurements, though the biases in ERA5 are smaller (King et al., 2022). Spatial differences within and between sectors are noticeable, and are not always consistent throughout the simulations, and therefore cannot be directly attributed to the changes in atmospheric forcing or sea ice model.

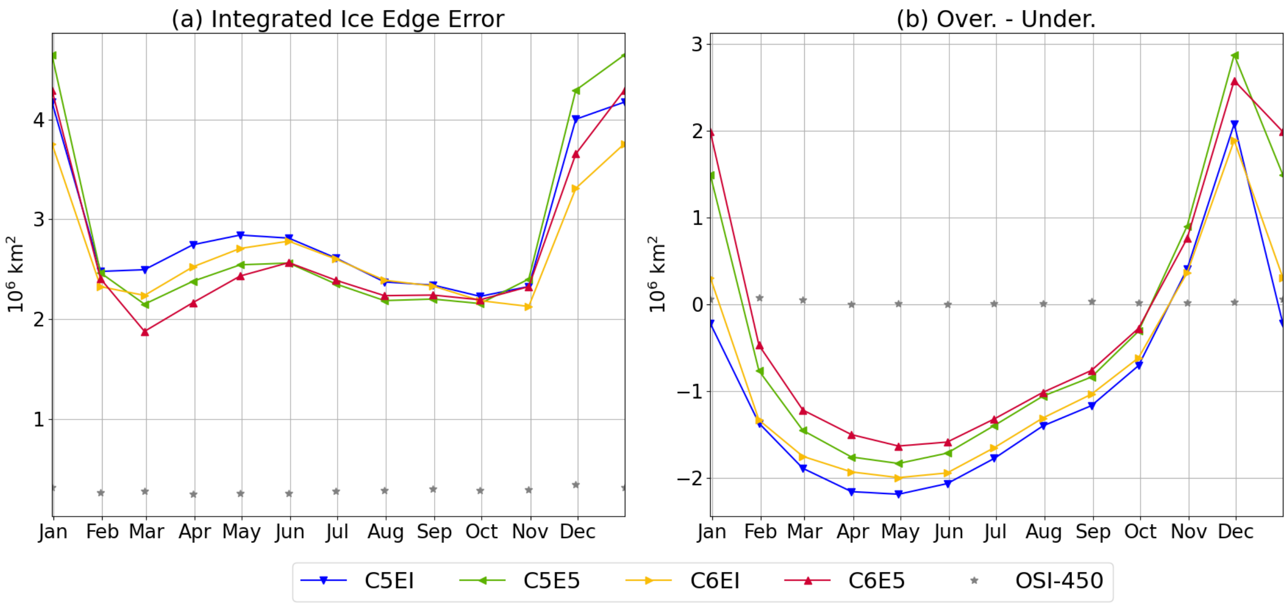

Figure 5. (a) Integrated ice edge error (IIEE) and (b) integrated ice edge overestimation-underestimation for all models compared to NSIDC CDR. Ice edge error for OSI-450 satellite measurements (grey stars) is presented to illustrate observational uncertainty. The analysis period is 1992–2018.

4.1.2 Sea ice edge

In addition to sea ice area and concentration, we look at the ice edge in the model and compare it to satellite measurements. 245 For this, we use the integrated ice edge error (IIEE), defined as the area where the model and the observations disagree on the ice concentration being above or below 15 %. The IIEE is calculated following Goessling et al. (2016), and using NSIDC CDR satellite observations as comparison:

$$\mathrm{IIEE} = O + U \tag{1}$$

where

250 $$O = \int_A \max(c_m - c_o, 0)\, dA \tag{2}$$

and

$$U = \int_A \max(c_o - c_m, 0)\, dA \tag{3}$$

A is the area of interest, here the Southern ocean, c=1 if the sea ice concentration is >15% and c=0 otherwise and m and o denote the model and the observations.

The smallest IIEE values are found between February–November for all model runs, with values ranging between 1.88–2.84×10^6 km^2. The largest IIEE is found from November to February, with maximum values in January (3.76–4.65×10^6 km^2). The simulations using ERA5 (C5E5 and C6E5) have a smaller IIEE (1.88–2.57×10^6 km^2) than the ERAI runs (2.23–2.84×10^6 km^2) from February to October. The CICE6 runs (C6EI and C6E5) have smaller values from February to June than the CICE5 runs (C5EI and C5E5), while from June to October both CICE versions have similar errors. From October to February, the C6EI run has the smallest error (2.13–3.76×10^6 km^2) and the C5E5 run the largest (2.16–4.65×10^6 km^2).

The difference between the ice edge overestimation minus the underestimation (Fig. 5b) indicates the direction of the IIEE. Positive values of this difference indicate a net overestimation of the ice edge in the model, suggesting an average ice edge located northward of the observed ice edge. Negative values indicate a net underestimation in the model, with the modelled ice edge located, on average, to the south of the observed ice edge. Further, values closer to zero indicate a good model performance in comparison to the observations in terms of the net ice edge. From February to October, the four model runs underestimate the ice edge (Fig. 5b). These results are consistent with the sea ice concentration and area underestimations found in summer (JFM), autumn (AMJ), and winter (JAS) in all model runs (see Fig. 2 and 3). These results indicate that the modelled ice edge from all simulations is located southward from the observed ice edge. As discussed in Sect. 4.1.1, the atmospheric forcing seems to play a larger role than the sea ice model, in this case, reducing the underestimation of the sea ice edge. Simulations forced with ERA5 (C5E5 and C6E5) result in a larger average sea ice extent than ERAI runs (C5EI and C6EI), better representing the ice edge conditions from the satellite observations between February–October. On the contrary, from November to January when an ice edge overestimation is observed from all model runs, the update in atmospheric forcing from ERAI to ERA5 increases the overestimation. The update from CICE5 to CICE6 results in smaller IIEE year-round for the simulations forced with ERAI, i.e. smaller underestimations between February–October and smaller overestimations in November–January (December for C5EI). The sea ice model update in ERA5 simulations results in an IIEE decrease, particularly between February–June; otherwise resulting in small improvements throughout the year.

4.1.3 Sea ice volume

Sea ice thickness observations are scarce and have large uncertainties (Holland et al., 2014; Uotila et al., 2019; Xu et al., 2021). For this reason, the sea ice volume results are assessed based solely on the comparison between the four different simulations using experiment C5EI as a baseline.

The total sea ice volume decreases due to the sea ice model update from CICE5 to CICE6, while the change in atmospheric forcing from ERAI to ERA5 has an opposite effect, resulting in the C5E5 simulation having the largest and C6EI the smallest volume in all seasons (Fig. 6). This is different from how the sea ice area behaves as both the sea ice model update and the atmospheric forcing update increase the area (see Sec. 4.1.1). The summer (JFM) is the season with the highest variability between simulations (Fig. 6a), as was the case for the area and concentration.

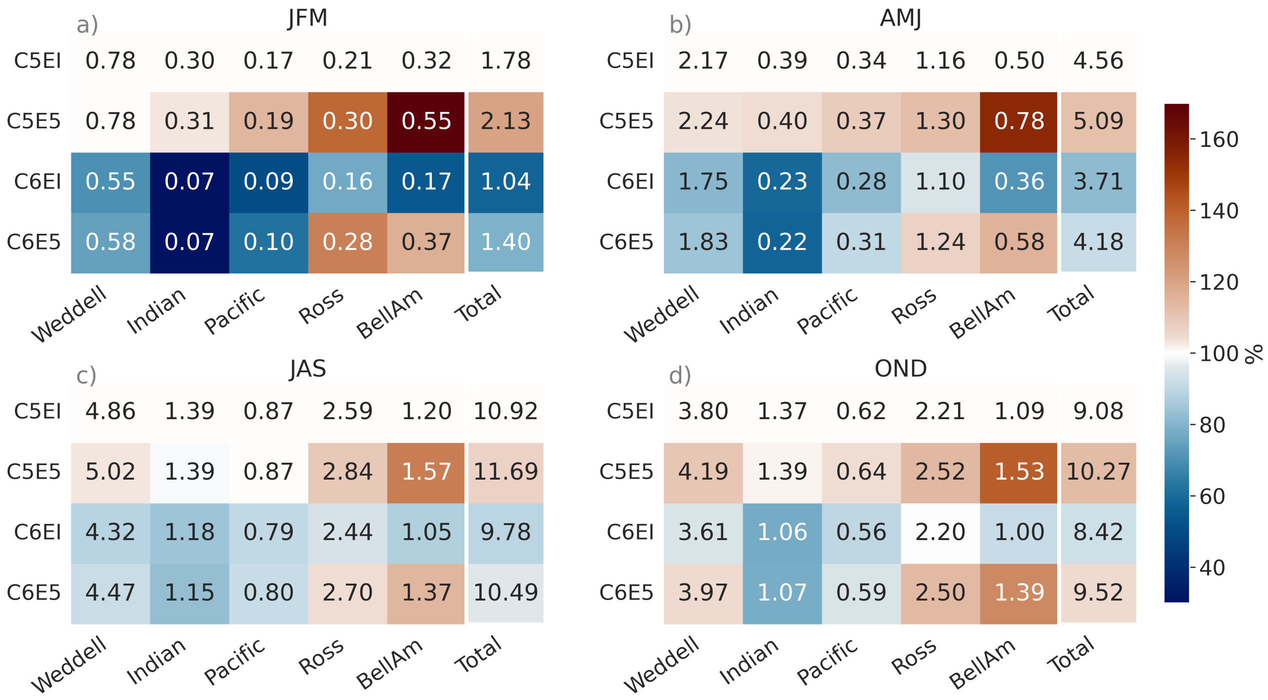

JFM

	Weddell	Indian	Pacific	Ross	BellAm	Total
C5EI	0.78	0.30	0.17	0.21	0.32	1.78
C5E5	0.78	0.31	0.19	0.30	0.55	2.13
C6EI	0.55	0.07	0.09	0.16	0.17	1.04
C6E5	0.58	0.07	0.10	0.28	0.37	1.40

AMJ

	Weddell	Indian	Pacific	Ross	BellAm	Total
C5EI	2.17	0.39	0.34	1.16	0.50	4.56
C5E5	2.24	0.40	0.37	1.30	0.78	5.09
C6EI	1.75	0.23	0.28	1.10	0.36	3.71
C6E5	1.83	0.22	0.31	1.24	0.58	4.18

JAS

	Weddell	Indian	Pacific	Ross	BellAm	Total
C5EI	4.86	1.39	0.87	2.59	1.20	10.92
C5E5	5.02	1.39	0.87	2.84	1.57	11.69
C6EI	4.32	1.18	0.79	2.44	1.05	9.78
C6E5	4.47	1.15	0.80	2.70	1.37	10.49

OND

	Weddell	Indian	Pacific	Ross	BellAm	Total
C5EI	3.80	1.37	0.62	2.21	1.09	9.08
C5E5	4.19	1.39	0.64	2.52	1.53	10.27
C6EI	3.61	1.06	0.56	2.20	1.00	8.42
C6E5	3.97	1.07	0.59	2.50	1.39	9.52

Figure 6. Seasonal mean sea ice volume [10^3 km^3] over 1992–2018 for the different sectors shown in Fig. 1b. The colour stands for the fraction of the area compared to the C5EI model run *([model area]/[C5EI area])*.

The increase in volume caused by the update of the atmospheric forcing to ERA5 is largest in the BellAm and Ross Sea sectors, where we can see an increase in volume in all seasons in both C5E5 and C6E5 (Fig. 6). The volume increase is especially large in C5E5 in the BellAm sector during summer (JFM) and autumn (AMJ) where there is a systematic increase in volume in the whole sector (Fig. A2e–h). The large increase in volume is especially noticeable at the Antarctic Peninsula, in both the BellAm and Weddell Sea sectors. However, in the Weddell Sea, the sea ice volume is smaller in C5E5 than in the C5EI baseline along the ice shelf edge, resulting in only a moderate net overestimation in the sector (Fig. 6 and Fig. A2e–h). The volume increase in C5E5 compared to C5EI is mostly consistent with the increase in sea ice concentration (Sect. 4.1.1, Fig. A1e–h). However, the small sea ice volume observed in the coastal region of the Weddell Sea is not followed by a decrease in concentration, indicating thinner ice.

The volume decrease caused by the sea ice model update is largest in the Indian Ocean sector, where a clear decrease in concentration is also seen (Sec. 4.1.1). Simulation C6EI consistently shows a smaller sea ice volume than the C5EI baseline in all sectors around the year (Fig. 6). The largest negative differences are observed along the coast across all sectors (Fig. A2i–l). Nevertheless, the sea ice volume is larger than in the baseline further away from the coast during spring (OND), resulting in a smaller net negative difference. In this simulation (C6EI), the volume and concentration patterns are not consistent, and only the summer (JFM) shows a decrease in both volume and concentration along the coast (Fig. A1i–l).

In C6E5, where both the atmospheric forcing and the sea ice model are updated, the difference from C5EI falls between C5E5 and C6EI. The total sea ice volume is less than in C5EI in all seasons except spring (OND) (Fig. 6), indicating that the update from CICE5 to CICE6 has a greater impact than the update of the atmospheric forcing. However, since C6E5 has a larger volume than C5EI in the Ross Sea and BellAm sectors throughout the year, it suggests that the atmospheric forcing has a stronger influence in these sectors. Similar to C5E5 and C6EI, the C6E5 simulation shows a smaller sea ice volume than C5EI close to the coast while further away from the coast it shows larger volumes than C5EI (Fig. A2m-p).

The increased concentration (see Sect. 4.1.1) but decreased volume when updating from CICE5 to CICE6, that we see in the difference between C6EI and C5EI (Fig. A2i–l and A1i–l), can be potentially caused by a difference in level ice area fraction (alvl) and ridged ice area fraction (ardg). C6EI has a larger alvl and smaller ardg than C5EI (Fig. A3). This means that the CICE6 model runs have less thick ridged ice and more thin level ice than the CICE5 model runs. The distribution of the difference in ardg (Fig. A3e–h) between the C6EI and C5EI shows similar patterns as the volume difference between the model runs, with the strongest decrease at the coast. Meanwhile, the difference in the distribution of alvl (Fig. A3)a–d) is similar to the difference in concentration, except around the coast where there is an increase in alvl from C5EI to C6EI in all seasons other than summer (JFM), that does not occur in the ice concentration. Ridging has been shown to increase sea ice volume (Zhang, 2014). Therefore, less ridging in C6EI is consistent with the smaller sea ice volume observed, while the large volume in C5EI, especially during winter, results from the larger ice growth in the open water regions caused by the ridging.

4.1.4 Sea ice drift

The sea ice drift was compared with two observational ice velocity products: 1) the Global Low Resolution Sea Ice Drift data record Release 1 from EUMETSAT (European Organisation for the Exploitation of Meteorological Satellites), hereafter OSI-455 (OSI SAF, 2022), with a spatial resolution of 75 km, and 2) the NOAA/NSIDC Polar Pathfinder Daily 25 km EASE-Grid Version 4, hereafter NSIDC ice drift (Tschudi et al., 2019). For NSIDC ice drift, the meridional velocity was multiplied with a constant factor of 1.357 to correct for its underestimated speed, as in Haumann et al. (2016).

All simulated and observed sea ice drift velocities are bilinearly interpolated onto a common polar stereographic grid with a resolution of 60 km to facilitate comparison. As satellite-derived ice velocities are often spatially smoothed to reduce the noise (Kimura et al., 2013), a 4 x 4 cell filter is first used to smooth the high resolution MetROMS-modelled ice velocities to ensure a comparable pattern with the observations.

Figure 7 shows the winter (JAS) climatological sea ice drift vectors and speeds. The two observational data sets are consistent in velocity direction, while NSIDC's ice speeds are consistently smaller than those of OSI-455. When comparing the model outputs with the observations, we should keep in mind that the coastal pixels are poorly resolved in the satellite data and are thus more uncertain.

As prescribed atmospheric forcing drives the model runs, the simulations generally captured the ice drift circulation patterns well (Fig. 7). For example, significant ice transport from the Ross shelf and transitions from the westward coastal drift to the eastward drift in the outer region, especially in the Ross Sea gyre and Weddell Sea gyre regions, can be seen. However, although the observations have considerable uncertainties near the Antarctic coast, clear overestimations can be seen. The larger speeds

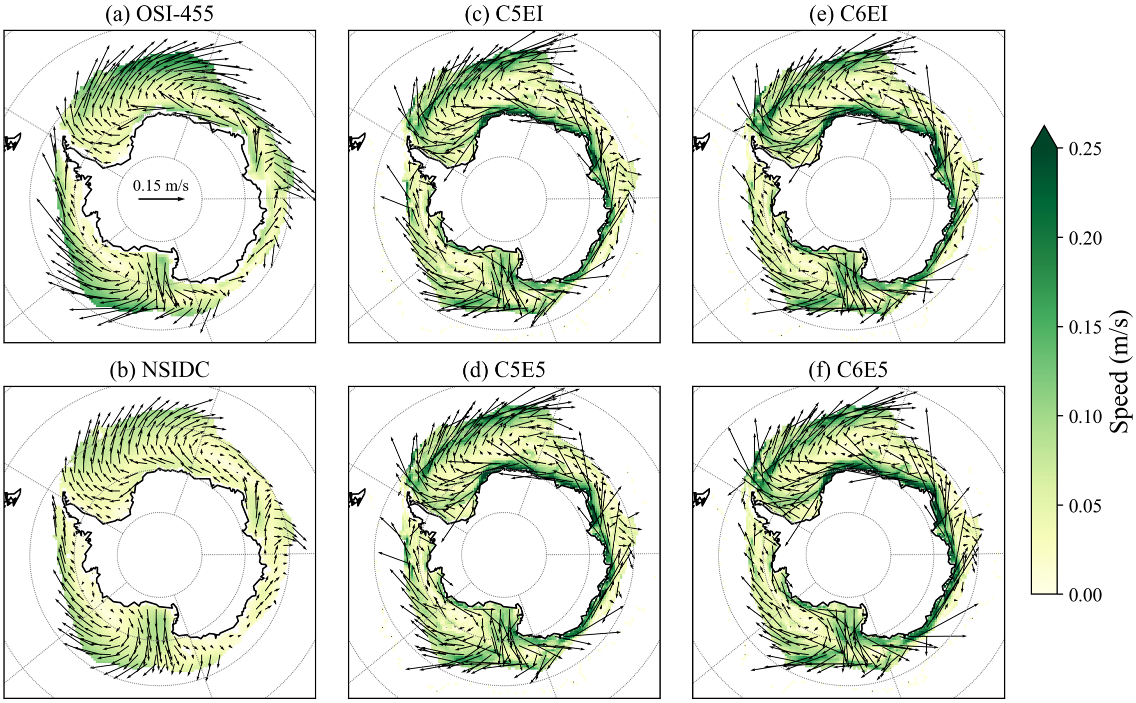

Figure 7. Mean sea ice velocities during winter (JAS) over the period 1992–2018, overlaid on the speed from (a) OSI-455, (b) NSIDC ice drift and (c–f) model outputs. Only grid cells with climatological sea ice concentration larger than 15 % are plotted.

in the model might occur due to the missing landfast ice component. Furthermore, the relatively low resolution of the ocean boundary at the coast and the lack of grounded icebergs could also contribute to the overestimation. A more complex ocean boundary including icebergs would, potentially, cause slower average motion of the sea ice and longer surviving ice in summer (Naughten et al., 2018b). The simple ocean boundary might also be a reason for the underestimation of the sea ice, especially in the summer, as it has been shown that sea ice transport is an important process during melt season (Goosse et al., 2023). There is no substantial change from updating the CICE5 to CICE6 or replacing the ERAI forcing with ERA5, except that the coastal ice motion speeds are increased by both updates, being the largest in the C6E5 run.

To quantify their similarities, we also compute the vector correlation coefficients (VCCs) between NSIDC/modelled ice drifts and the OSI-455 using the Sea Ice Evaluation Tool (Lin et al., 2021) (Fig. 8). Both NSIDC and simulations show higher VCCs with OSI-455 in the western geographical sectors (Ross Sea, BellAm, and Weddell Sea) than in the east (Indian and Pacific Oceans). The correlation is particularly high in the areas of the Ross Sea gyre and the Weddell Sea gyre. Quantitatively, the improvements from replacing ERAI with ERA5 are now clearer than those shown in Fig. 7, with robust increases in VCCs for all sectors other than the Pacific Ocean. Updating the sea ice model from CICE5 to CICE6 gives a larger improvement than updating the atmospheric forcing, especially in the BellAm sector, the Ross Sea gyre, and the Weddell Sea gyre. The overall consistency between NSIDC and OSI-455 (0.590) is only slightly higher than between the simulations and OSI-455

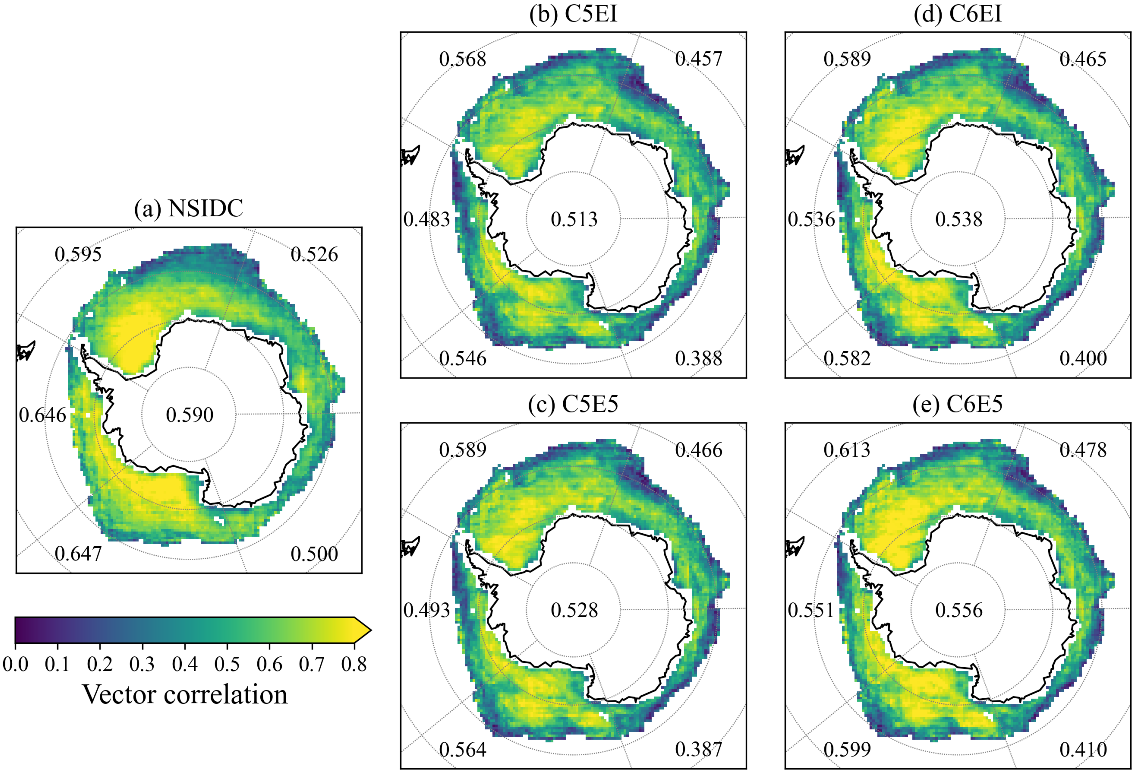

Figure 8. Significant ice drift vector correlation coefficients from monthly mean data during 1992–2018 at a confidence level of 99% between OSI-455 data and (a) NSIDC ice drift and (b–e) model outputs. The mean correlation coefficients for each geographic sector are listed in their respective positions, with the value in the centre of the figure representing the pan-Antarctic mean.

(0.513–0.556), and not as pronounced as in the visualization of Fig. 7. C6E5 shows the highest correlation of the model runs, and C5EI is the lowest.

4.2 Oceanic variables

4.2.1 Ocean Hydrography

Oceanic heat content and basal melt are influenced by currents and water mass properties, which are, in turn, influenced by the sea ice and the atmosphere. In this section, we investigate the water mass properties on the continental shelf, south of 65° S (Fig. 9) and in the upper 1500 m over the entire Pan-Antarctic domain (Fig. 10). For this, we compare the model simulations to the 1° gridded analysis of the observational dataset EN4.2.2 (Good et al., 2013) ensemble members using Gouretski and Cheng (2020); Gouretski and Reseghetti (2010) bathythermograph corrections (later referred to as EN4). This dataset is maintained by the Met Office Hadley Centre for Climate Change and provides comprehensive subsurface ocean temperature and salinity (vertical profiles and monthly objective analyses), integrating several data sources.

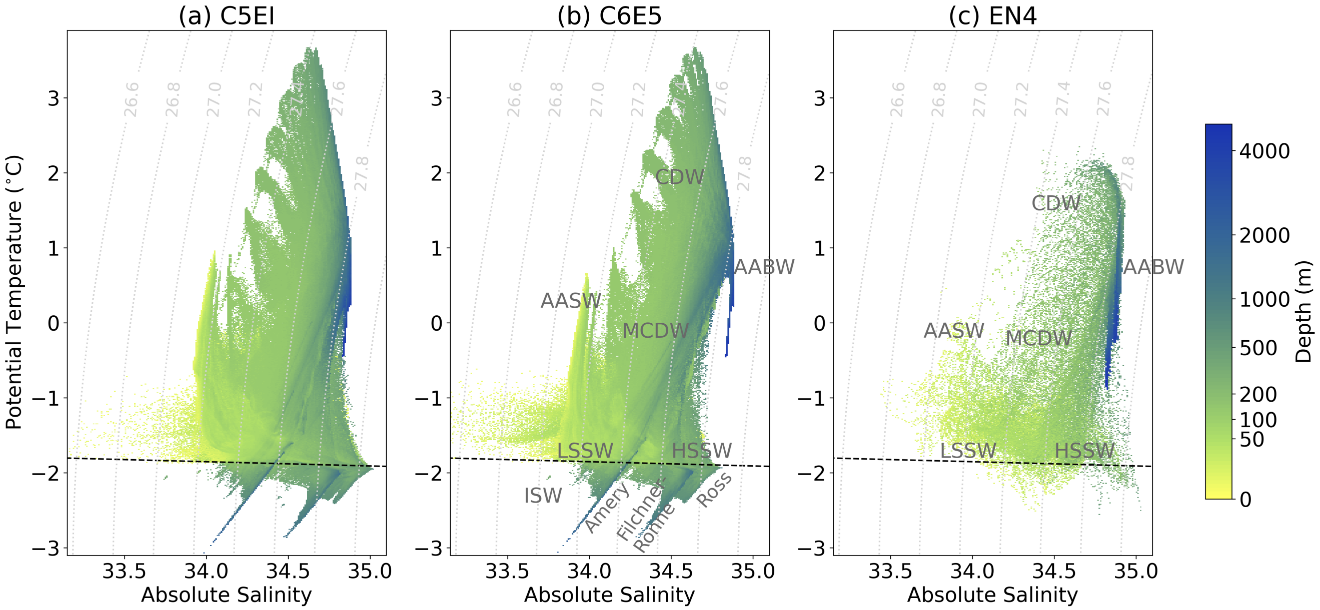

Figure 9. Modelled average 1992–2018 TS-diagrams for (a) C5EI, (b) C6E5 and (c) observed EN4 on the continental shelf (south of 65° S). Depth indicates the average depth of a given temperature–salinity value. The surface freezing point is marked with the dashed line. Water masses are marked in grey on the figure in the middle: AABW: Antarctic Bottom Water, CDW: Circumpolar Deep Water, MCDW: Modified Circumpolar Deep Water, LSSW: Low-Salinity Shelf Water, HSSW: High-Salinity Shelf Water, AASW: Antarctic Surface Water, and ISW: Ice Shelf Water.

On the continental shelf, all major water masses can be identified from the simulations (Fig. 9). Here, only model runs C5EI and C6E5 are shown as the main differences come from the upgrade from CICE5 to CICE6, while changes from ERA5 to ERAI are relatively small (not shown). The overall shape of the modelled TS-diagrams looks similar. However, the Ice Shelf Water (ISW), the High-Salinity Shelf Water (HSSW), the Low-Salinity Shelf Water (LSSW), and the Modified Circumpolar Deep Water (MCDW) are consistently fresher in CICE6 compared to CICE5 runs (Fig. 9a, b).

Below the surface freezing point (dashed lines in Fig. 9) lies the ISW. This water mass can be this cold without freezing because it is located under the ice shelves, where the high pressure lowers the freezing point. The water under the ice shelves follows the diagonal dilution ratio of melting and freezing seawater (Gade, 1979). The ice shelf waters have different salinity, which can be used to differentiate them. The three biggest ice shelves in Antarctica are (in order of decreasing salinity): the Ross, the Filchner-Ronne, and the Amery ice shelf. All of them clearly fresher in the C6E5 than in the C5EI run (Fig. 9).

The surface (above 100 m), which consists of Antarctic Surface Water (AASW), generally has salinity lower than than 34.5 overlying the higher salinity subsurface waters. Salinity can be below 33.5 in the narrow embayments in the BellAm sector. Temperature is mostly below 0°C except in the BellAm sector. Surface waters that are more saline than 34.5 with temperatures around -1°C can be found in the Ross Sea polynya. These waters are less saline in the CICE6 runs than in the CICE5 runs.

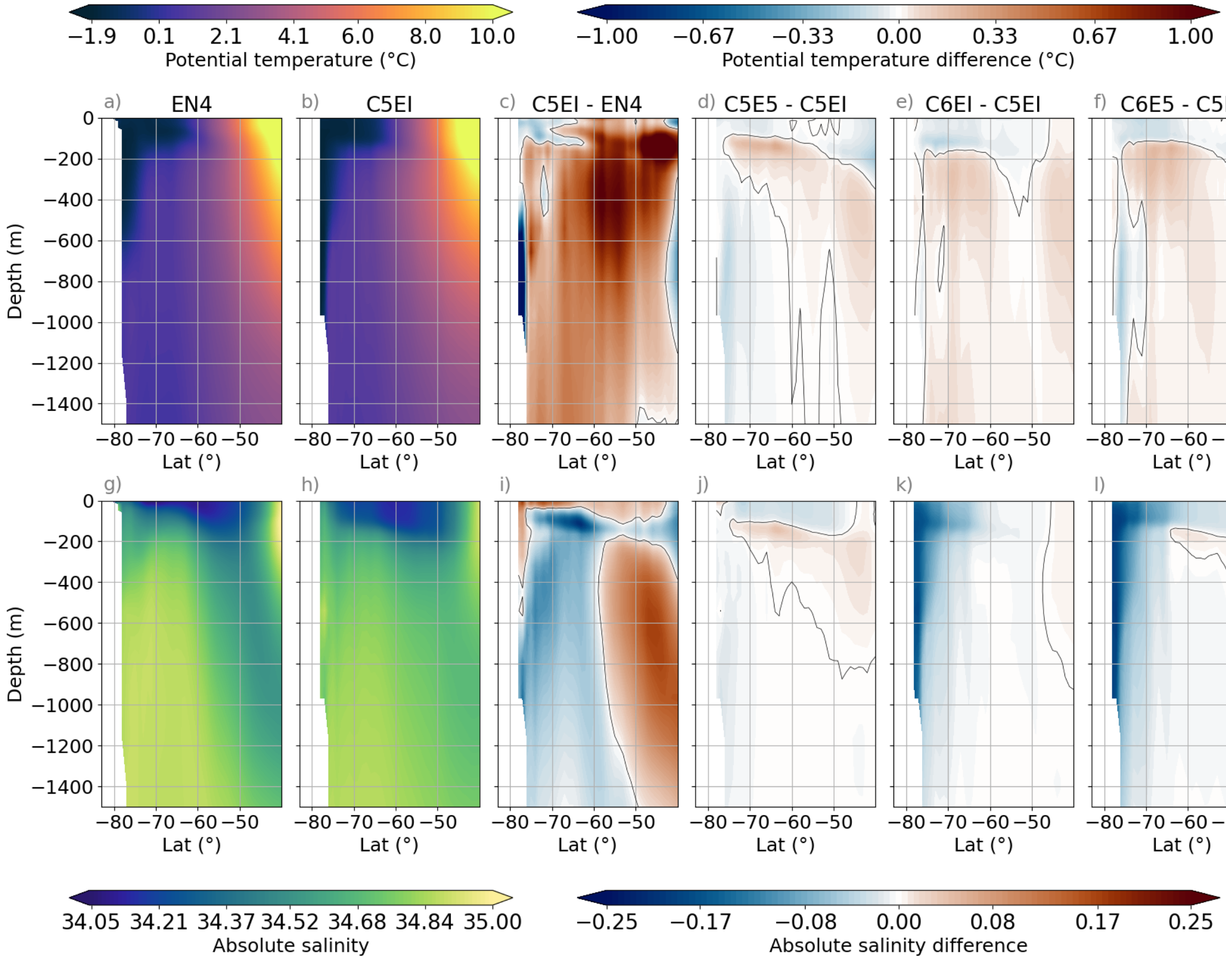

Figure 10. Pan-Antarctic zonal average of the 1992–2018 mean temperature and salinity from the upper 1500 m for EN4 observations (a, g), model run C5EI (b, h), difference between them (C5EI–EN4) (c, i) and model run differences C5E5-C5EI (d, j), C6EI-C5EI (e, k) and C6E5-C5EI (f, l). The grey contours in c–f (i–l) indicate a zero potential temperature (salinity) difference. Simulations have been integrated to the EN4 grid, meaning ice shelf cavities have been left out of the plot.

Just above the surface freezing point is the cold subsurface (∼100–500 m) shelf water which is the result of sea ice formation. This water is divided into HSSW (salinity > 34.62: Miller et al. (2024)) and LSSW. Similar to the ISW, these water masses are fresher in C6E5 than in C5EI. Furthermore, CICE6 has a smaller salinity range between HSSW and LSSW, as the CICE6 to CICE5 HSSW salinity difference is larger than the CICE6 to CICE5 LSSW one. In general, these cold shelf bottom waters are less saline in the model than in EN4 (Fig. 9). Since EN4 data are quite sparse, we also compare the simulated shelf bottom salinity and temperature to the Schmidtko et al. (2014) climatology, compiled from seven publicly available CTD datasets (Fig. A4). This comparison confirms that the CICE6 model runs are fresher than the observations.

Deep waters take a long time to spin up due to longer residence times, as discussed in Sect. 3.1, and should therefore be interpreted with caution. The deepest waters, below 1000 m, corresponding to the Antarctic Bottom Water (AABW), have salinity above 34.6 in all simulations (Fig. 9). The deepest, most saline parts of AABW are similar in all model runs, and are slightly warmer than in EN4, while the shallower parts of the AABW have a larger spread in salinity in the CICE6 simulations than the CICE5 simulations. Above the AABW, on the continental slope, the fresher and warmer Circumpolar Deep Water (CDW) can be identified. The warmest CDW is located in the BellAm sector with modelled temperatures of up to 3°C, which are clearly warmer than in EN4 (Fig. 9). The model runs tend to be slightly warmer than EN4 in all the other sectors as well. The CDW mixes with other water masses and produces the cooler Modified CDW (MCDW), also noticeable in Fig. 9.

Pan-Antarctic zonal mean temperature and salinity are illustrated in Fig. 10. We focus our analysis on the top 1500 m as changes in the deeper ocean are small, and uncertain due to the short spinup. The temperature distribution is similar between EN4 and C5EI (Fig. 10a, b), but C5EI is warmer than EN4, except for the southernmost parts and above 200 m depth south of 60° S (Fig. 10c). Atmospheric forcing and sea ice model upgrades thus both contribute to a decrease of temperature in the upper ocean (Fig. 10d–f). Differences between C5E5 and C5EI also show a temperature increase below the mixed layer, with the maximum warming at $\sim$150m in coastal areas (65° S), and a slight cooling below that and to the south (Fig. 10d). The upgrade to CICE6 leads to uniform warming of the ocean interior (Fig. 10e,f).

The vertical salinity gradient is weaker in the model simulations than in EN4 south of 60° S (Fig. 10g–i). The surface is more saline in the model run C5EI than in EN4 and less saline below the surface and south of 60° S with the largest negative difference in salinity at around 100 m depth between 60–70° S (Fig. 10i). Northward of 60° S, the relatively fresh Antarctic Intermediate Water (AAIW) is clearly visible in both EN4 and the models, but is much saltier in the models below 200 m depth. Updating the atmospheric forcing from ERAI to ERA5 slightly increases the gradient, freshening the surface slightly and increasing the salinity in the interior (Fig. 10j). The change of the sea ice model from CICE5 to CICE6 results in a clear freshening in the south (Fig. 10i), in line to what we could see on the shelves (Fig. 9). This freshening is also visible in the ice shelf cavities (not shown). CICE6 runs, therefore, have an increased fresh bias, with salinity values further away from the observations than CICE5 runs. The bias can be attributed to the salt flux from CICE to ROMS which is, on average, smaller in CICE6 than in CICE5. The largest differences can be found at the coast and when the salinity flux is positive, i.e. from the ice towards the ocean (not shown). A way to mitigate the freshening problem in MetROMS-UHel could be to update the salinity restoration scheme. The current salinity restoration scheme is only applied when the ocean is deeper than 1500 m (Sect. 3.2) and does not take sea ice into account. Testing different salinity restoration schemes is beyond the scope of this work.

4.2.2 Mixed layer depth

A correct representation of the mixed layer depth (MLD) is of fundamental importance to reproduce air–sea exchanges and to adequately depict the oceanic heat loss in winter. Regions of strong sea ice formation usually have wintertime deep water formation due to brine rejection. These processes have consequential effects on water mass properties. To validate the model runs, we compare monthly MLD values obtained from the simulations to the 50-years (1970–2018) observational MLD climatology (Sallée et al., 2021a), described in Sallée et al. (2021b). It is important to note that this dataset only overlaps with

https://doi.org/10.5194/gmd-2024-213
Preprint. Discussion started: 13 December 2024

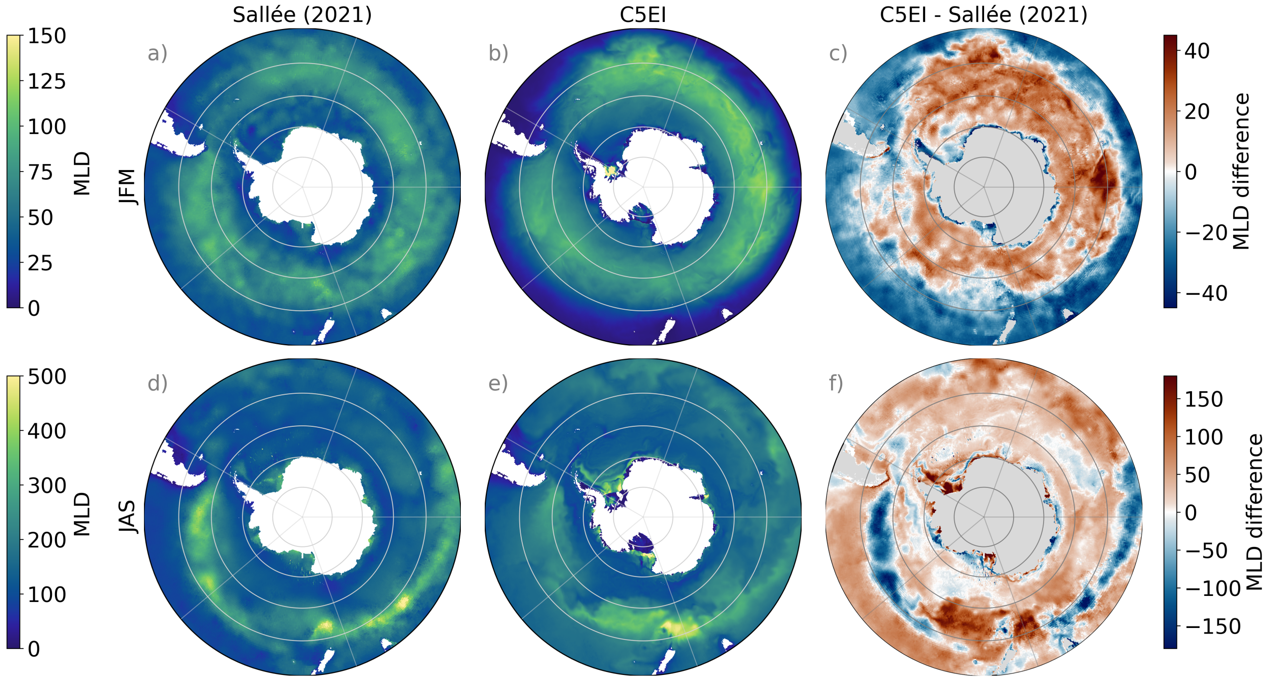
Sallée (2021)

C5EI

C5EI - Sallée (2021)

Figure 11. Summer (JFM) and winter (JAS) mixed layer depth (MLD) in meters. From left to right; Sallée et al. (2021a) climatology (a, d), C5EI simulations (b, e) and the difference between C5EI simulation and Sallée et al. (2021a) (c, f). The (Sallée et al., 2021a) climatology is calculated from observations 1970–2018 and the model runs are from 1992–2018. Note the different scales on colour bars for summer and winter.

our experiments during the period 1992–2018. The MLD is calculated using a density (σ) criterion, as the depth at which the difference with the surface density is equal to 0.03 kg m^{-3}, following the same method of (Sallée et al., 2006, 2013).

The large scale patterns of the MLD are well reproduced (Fig. 11). In summer (JFM) the ACC (∼60–50° S) is clearly recognizable as the area of deeper MLD (up to ∼100 m) (Fig. 11a, b). In this region, the modelled results tend to overestimate (∼40 m) the MLD (Fig. 11c). On the other hand, the MLD is underestimated on the outer part of the domain (north of ∼50° S), as well as on most of the continental shelf. Changing the forcing from ERAI to ERA5 mitigates some of these biases. The MLD overestimations in the open ocean decrease with the updated atmospheric forcing, with smaller MLD in C5E5 than in C5EI along the ACC (Figs 12a). This decreased MLD in the open ocean is likely due to the larger vertical salinity gradient at the surface discussed in the previous section and shown in Fig. 10j. Furthermore, on the continental shelf, there is a decrease in the underestimation after the atmospheric forcing update, with deeper MLD values in C5E5 than in C5EI. Exceptions to this pattern occur under the Filchner-Ronne Ice Shelf in the Weddell Sea where a strong shallowing of the MLD is observed in C5E5 (Fig. 12a). The sea ice model update produces a small increase of the MLD (Fig. 12b), particularly in the southernmost areas of the domain. The final set up with both upgrades implemented displays, therefore, a small improvement of the summer MLD with decreased MLD in the open ocean and increased MLD at the continental shelf (Fig. 12c).

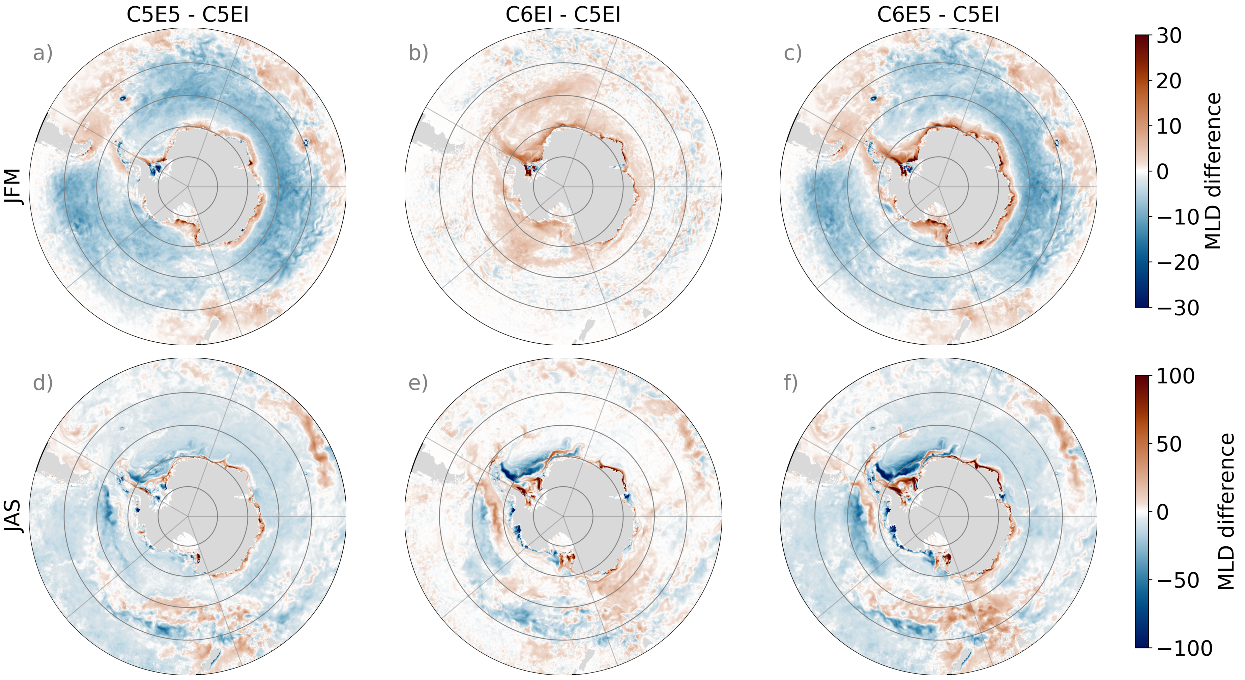

Figure 12. Summer (JFM) and winter (JAS) mixed layer depth (MLD) difference between models C5E5-C5EI (a, d), C6EI-C5EI (b, e) and C6E5-C5EI (c, f). Note the different scales on colour bars for summer and winter and different from Figure 11.

Winter (JAS) MLD is larger than in summer, reaching depths over 400 m in some regions along the northern boundary of the ACC, through the BellAM, Ross Sea, and Pacific sectors, to the eastern part of the Indian Ocean (Fig. 11d). This pattern is also captured in C5EI (Fig. 11e), but the band of increased MLD is not as pronounced as in the observations. This is mostly caused by a general overestimation of MLD values over the domain, as well as by a seasonal signal over the ACC, where there is a negative bias and the MLD does not deepen as much as in the observation (Fig. 11f). The areas close to Tasmania and New Zealand are an exception, where the ACC has a strong positive bias. The MLD underestimation could be explained by the lack of sinking AAIW in the models (Fig. 10i). The difficulty of preserving AAIW in MetROMS has earlier been discussed in (Naughten et al., 2018b) and has been attributed to spurious diapycnal mixing with a potential contribution from errors in the surface forcing. The spurious diapycnal mixing and the drift in the density structure due to non-closure of the freshwater budget leads to a degradation of the Southern Ocean interior water masses, and to for example a weakening ACC (not shown). The biases have a more complex pattern over the continental shelf, with mostly shallower MLD (Figs 11f), and a few areas with high positive bias and possible deep water formation (e.g. next to the Ross, Filchner-Ronne, and Amery Ice shelves).

Updating the atmospheric forcing from ERAI to ERA5 slightly decreases the wintertime MLD over most of the model domain, especially in the Weddell Sea sector at ∼70° S (just off the shelf) and in the BellAm sector a bit south of 60° S (Fig. 12d). Along the shelf, on the contrary, the update slightly increases the wintertime MLD, especially in the Weddell Sea, Indian Ocean, and Pacific Ocean sectors, in a similar way as it does in the summer. Updating the sea ice model from CICE5 to CICE6

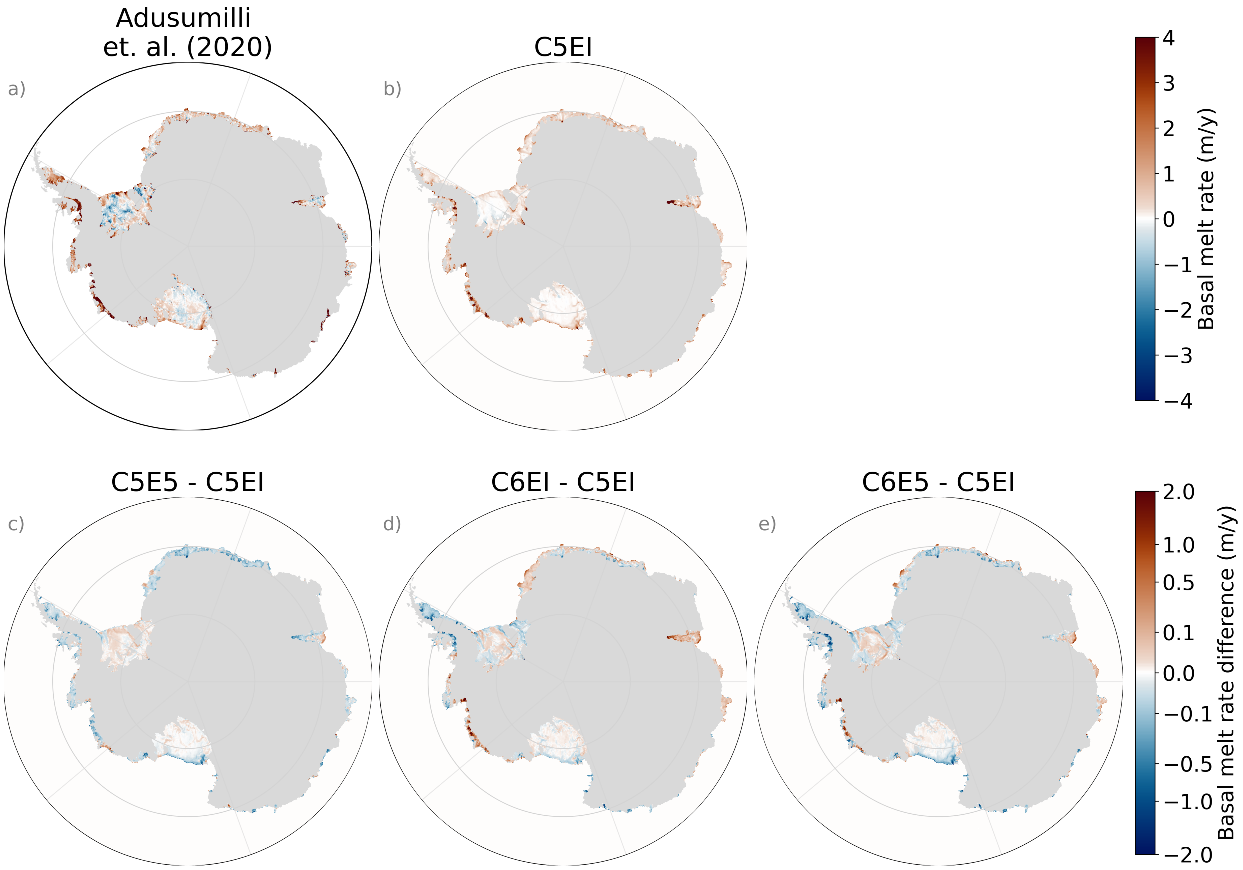

Figure 13. Map of annual average melt rate (m yr^{-1}) for (a) observational estimate from Adusumilli et al. (2020), (b) C5EI model run, and (c–e) difference between the C5EI model run and the other model runs. The model run averages are calculated from 1996–2018. Note that differences have a different colour scale.

results in a slightly deeper MLD along the shelves in most of the Weddell Sea, Indian Ocean, and western Ross Sea sectors, and a shallower MLD on the shelf in the east Ross Sea and BellAm sectors (Fig. 12e). There are no additional effects from updating both the atmospheric forcing and sea ice model (Fig. 12f).

4.3 Ice shelf basal melt

450 Basal melting of the Antarctic ice shelves is an important source of freshwater to the Southern Ocean. To validate the model results we compare to Adusumilli et al. (2020) estimates of total meltwater flux from the basal melt of the Antarctic ice shelves from 1994 to 2018. Adusumilli et al. (2020), assuming a steady state, calculated a total flux of 1100±60 Gt yr^{-1}. These estimates were done using CryoSat-2 radar altimetry, satellite-derived ice velocities, a model of surface mass balance, and firn

state variability. Our model runs reach equilibrium in 1996 (Fig. A5), and thus the average melt rates for the model simulations are calculated over the 1996–2018 period.

All the model runs underestimate the total ice shelf basal mass loss compared to observations by, approximately, a factor of two. The simulated loss averaged over 1996–2016 are 578 Gt yr^{-1} for C5EI, 538 Gt yr^{-1} for C5E5, 599 Gt yr^{-1} for C6EI and 546 Gt yr^{-1} for C6E5. Updating the atmospheric forcing from ERAI to ERA5 has a decreasing effect, while updating the sea ice model slightly increases the flux.

The map of the average melt rate shows that the model bias is regional (Fig. 13). For example, the Filchner-Ronne ice shelf, in the Weddell Sea, is melting both at the front and at the grounding line with refreezing in the centre and the west. The refreezing in the middle is underestimated and the melting at the front is excessively small. A similar, but smaller, underestimation of refreezing and melting can be seen in the Ross ice shelf. Underestimations of modelled melt rates can also be seen at the ice shelves in the BellAm sector in west Antarctica, and in the Pacific sector.

After changing the atmospheric forcing from ERAI to ERA5 (Fig. 13c) melt rates decrease in most areas. The change from CICE5 to CICE6 13d) shows rather varying regional response, with the highest melt increase in the Amundsen Sea. Melt rates also increase in front of Dronning Maud Land in the Weddell Sea sector and in front of the Amery ice shelf in the Indian Ocean sector. Melt rates decrease in west Antarctica, on both sides of the Antarctic Peninsula, as well as close to the border of the Ross Sea and Pacific Ocean sectors. When combining both ERA forcing and CICE model updates, as in C6E5, melt rates increase in the Amundsen Sea, in parts of the Weddell Sea sector, and at the Amery ice shelf, but decrease at the Antarctic Peninsula, in the Dronning Maud Land, in the Pacific sector, and in front of the Ross ice shelf (Fig. 13e).

Even though the differences between the models and observations are regional, there is still a systemic bias for which there are two likely reasons: tides and spatial resolution. Both the MetROMS-Iceshelf and MetROMS-UHel models lack tides, which have been shown to be important for glacier mass loss in the Antarctic, most importantly through efficient tidal mixing of heat and subsequent ice shelf basal melting. (Padman et al., 2018). Boeira Dias et al. (2023) showed that tides affect water mass transformation under some ice shelves. As the heat and salt transfer is dependent on velocities at the base of the ice shelf base, it is expected that tidal currents would increase melt in ice shelf cavities. The low horizontal resolution likely also causes an underestimation of the basal melt rate due to the underestimated transport of warm CDW onto the continental shelf. For example, in the BellAm sector at the western Antarctic Peninsula, observations suggest that the mechanism for the transport of warm CDW onto the shelf is related to eddies shed from the ACC (Martinson and McKee, 2012). These eddies are not fully resolved with the resolution of our model. Additionally, Nakayama et al. (2014) shows that a resolution of at least 5 km is required over the continental shelves to resolve the mean flow topography interaction, needed for realistically simulated CDW intrusion in the BellAm seas. A clear cold bias in the bottom water temperatures compared to the Schmidtko et al. (2014) observations is visible (Fig. A4b, c) in the BellAm sector, indicating that the lack of CDW intrusion is indeed the likely reason for the low melt rates and bottom temperatures we see in the BellAm sector in our models.

5 Conclusions

We present the MetROMS-UHel ocean–sea ice model, and how the modelling results have changed with the updated ERA atmospheric forcing and the sea ice model CICE compared to the MetROMS-Iceshelf model. Overall the new model has a better representation of the sea ice than the older version. Specifically the MetROMS-iceshelf model underestimates the sea ice concentration and area compared to observations, but in the MetROMS-UHel model this negative bias is reduced. For the sea ice volume, where no observations are available for comparison, the model showns an increases with the ERA update, but a decrease with the CICE update for a very small combined effect. Both model versions capture the sea ice drift patterns well, but the vector correlation shows a slight improvement in MetROMS-UHel by both the ERA and the CICE update. In the ocean, both model versions are able to identify the main water masses on the shelf, though with a positive bias in interior ocean temperatures (compared to observations). Furthermore, MetROMS-iceshelf overestimate the MLD in the deep ocean while underestimating MLD on the shelf. The ERA update slightly reduce these biases in MLD. The CICE update, on the other hand, causes a clear decrease in coastal salinity, resulting in a negative salinity bias in MetROMS-UHel. Adjusting the configuration of the coupled ROMS–CICE6 model under the ERA5 forcing is required to mitigate this effect (Barthélemy et al., 2018). In the ice shelf cavities, MetROMS-iceshelf underestimate melt rates by approximately a factor of two, which is attributed to a low model resolution and missing tides. In MetROMS-UHel the ERA update increases the underestimation, while the CICE update slightly decreases it. However, the effect of the updates is very small and regionally varying. Overall, both the atmospheric forcing and the sea ice model update improve the model system, with the ERA update having on average a stronger effect on sea ice area, concentration, and basal melt rate, while the CICE update has a stronger effect on the sea ice volume, drift, and the ocean hydrography. However, the amount and direction of changes vary regionally, suggesting that the importance of physical processes and external forcing depends on the region.

Code and data availability. MetROMS-Iceshelf model code is available at https://doi.org/10.5281/zenodo.1157229 (Naughten et al., 2018a), MetROMS-UHel model code is available at https://doi.org/10.5281/zenodo.14185734 (Äijälä and Uotila, 2024) and code for analyzing the model output as well as relevant model data to produce the figures can be found at https://zenodo.org/records/14186139 (Äijälä and Nie, 2024).

510 ## Appendix A: Additional figures

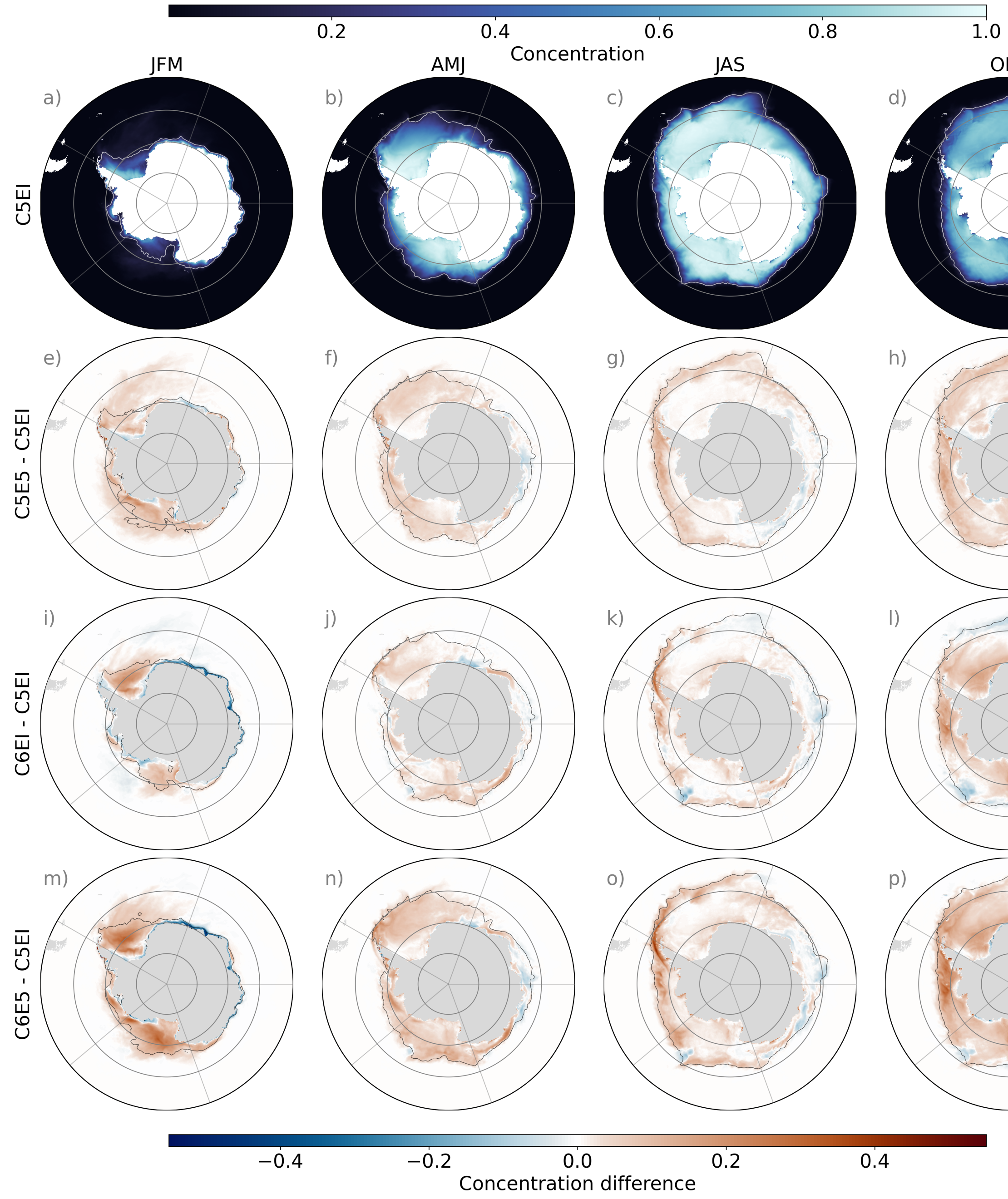

Figure A1. Sea ice seasonal mean concentration over the period 1992–2018 from model run C5EI (a–d) and concentration differences (e–p) between C5EI and the other model runs (C5E5, C6EI, C6E5). The black (white) line shows the sea ice extent.

https://doi.org/10.5194/gmd-2024-213
Preprint. Discussion started: 13 December 2024

Geoscientific Model Development
Discussions

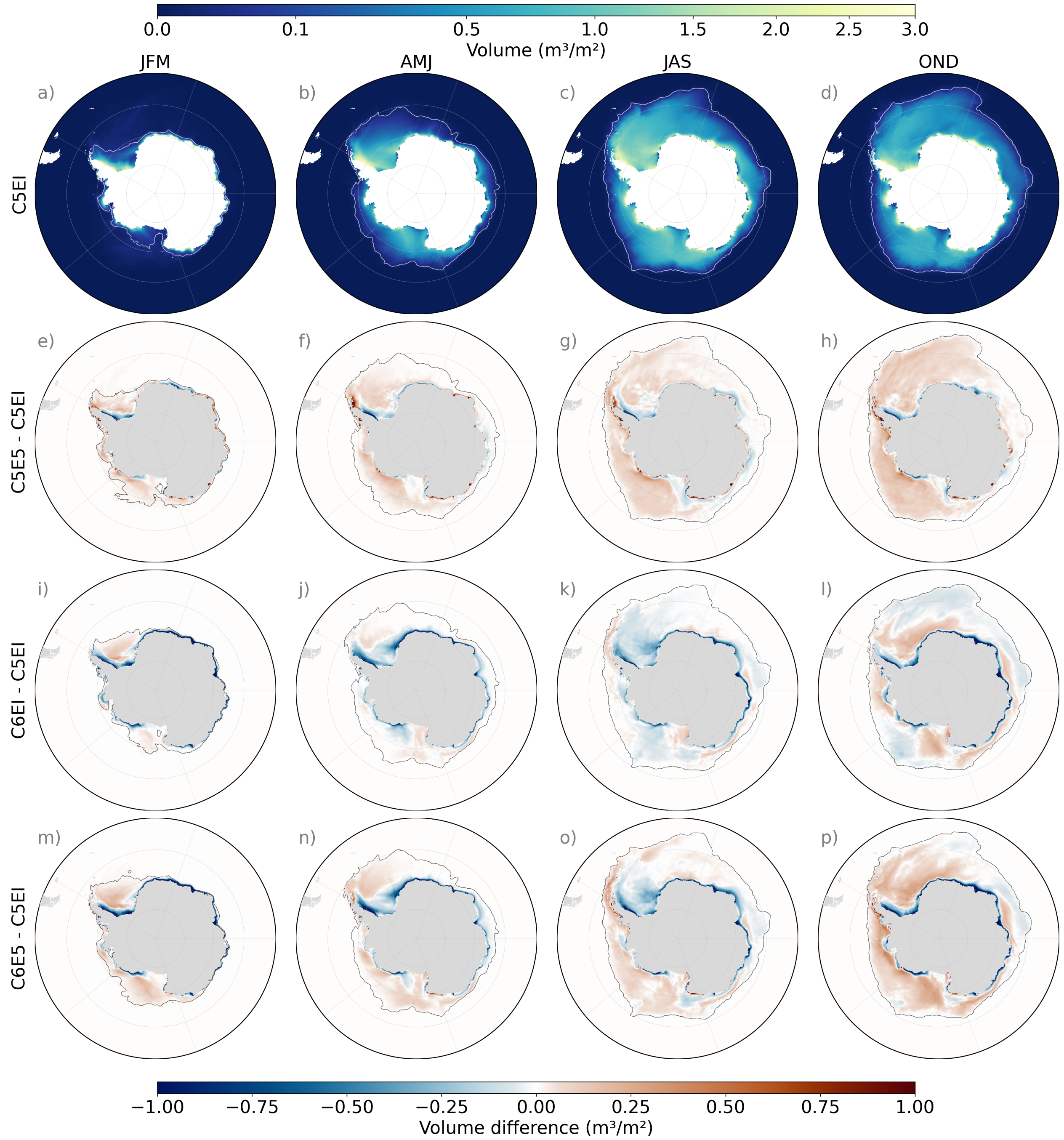

Figure A2. Sea ice seasonal mean volume [m^3/m^2] over 1992–2018 from model run C5EI (a–d) and volume differences (e–p) between C5EI and the other model runs (C5E5, C6EI, C6E5). The black (white) line shows the sea ice extent.

https://doi.org/10.5194/gmd-2024-213
Preprint. Discussion started: 13 December 2024

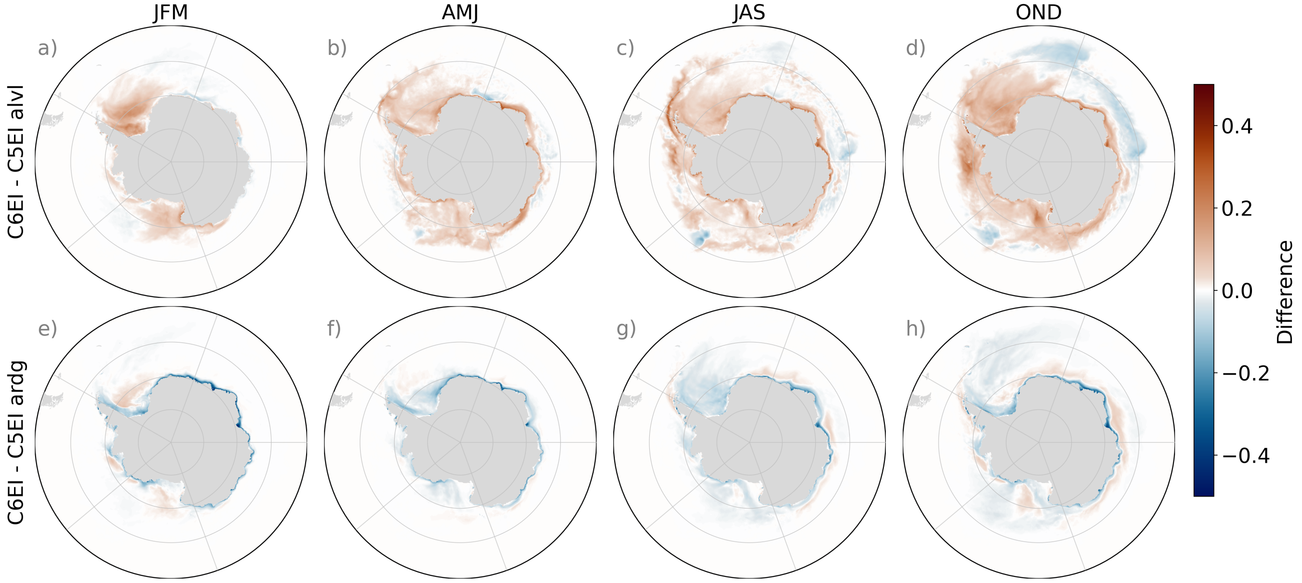

Figure A3. Difference of level ice area fraction (alvl) (a–d) and ridged ice area fraction (ardg) (e–h) between the C6EI and C5EI simulations. Values are seasonal means from 1992–2018.

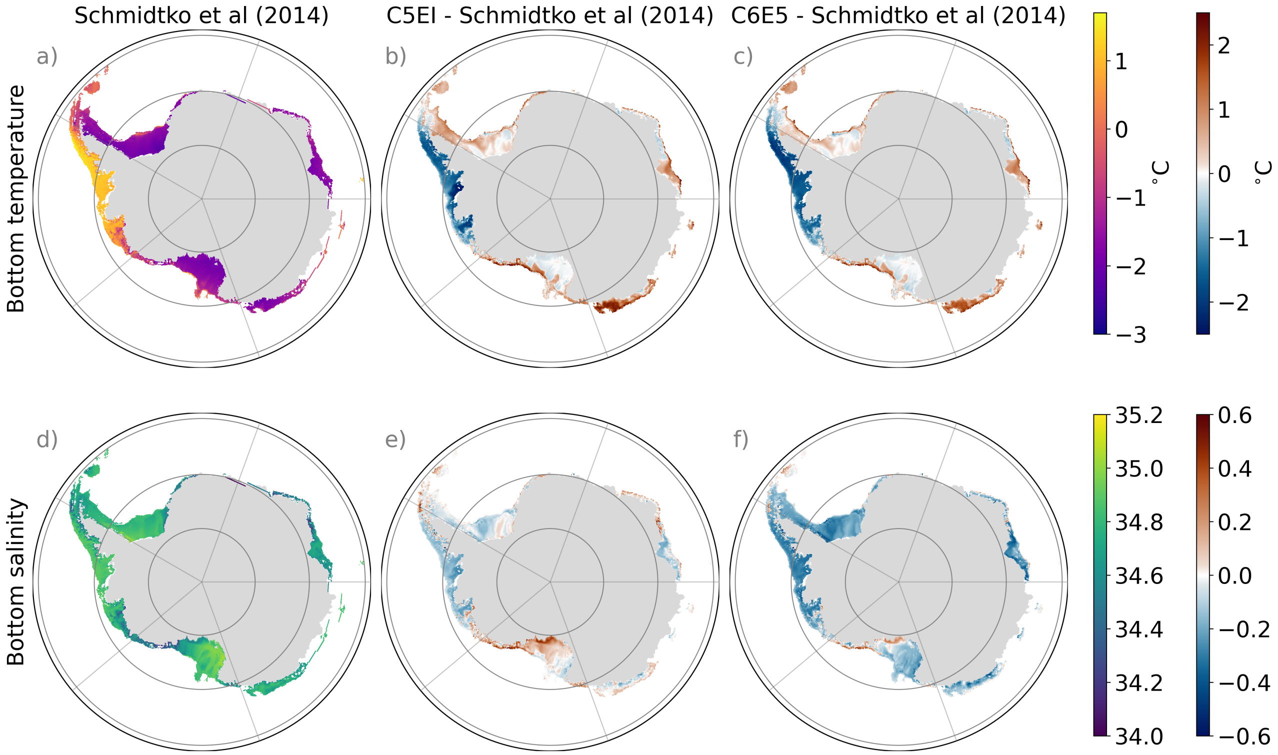

Figure A4. (a) Annual average bottom potential temperature (°C), (d) salinity, both from Schmidtko et al. (2014), and (b, e) the difference between the model run C5EI and Schmidtko et al. (2014), and (c, f) C6E5 and Schmidtko et al. (2014). The period considered is 1992–2012.

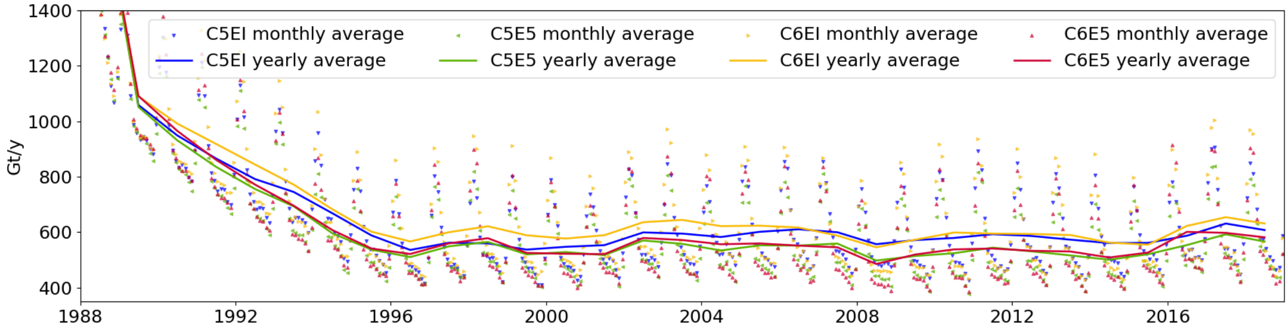

Figure A5. Timeseries of melt rate from the different model runs C5EI (blue), C5E5 (yellow), C6EI (green), and C6E5 (red) from the start of the spinup. The years 1988 to 1991 stand for the spinup with year 1992 forcing. Solid lines show yearly averages and dots show monthly averages. The models take until 1996 to find a balance.

Author contributions. **Cecilia Äijälä:** Conceptualization, Methodology, Software, Validation, Formal analysis, Investigation, Data Curation, Writing - Original Draft and Review & Editing, Visualization. **Yafei Nie:** Methodology, Software, Validation, Formal analysis, Writing - Original Draft (Sea Ice Drift), Review & Editing, Visualization. **Lucía Gutiérrez-Loza:** Writing - Review & Editing. **Chiara De Falco:** Writing - Review & Editing. **Siv Kari Lauvset:** Writing - Review & Editing, Funding acquisition **Bin Cheng:** Writing - Review & Editing **David A. Bailey:** Writing - Review & Editing **Petteri Uotila:** Conceptualization, Resources, Writing - Review & Editing, Supervision, Project administration, Funding acquisition.

Competing interests. The authors declare that they have no conflict of interest.

Acknowledgements. This study was undertaken as part of the EU Horizon 2020 PolarRES project (https://polarres.eu), funded under grant agreement number: 101003590. The authors thank the EU commission for facilitating this research. Additionally Yafei Nie was supported by the China Postdoctoral Science Foundation (Grant No. 2023M741526) The authors wish to acknowledge CSC – IT Center for Science, Finland, for computational resources. EN.4.2.2 data were obtained from https://www.metoffice.gov.uk/hadobs/en4/ and are © British Crown Copyright, Met Office, 2024, provided under a Non-Commercial Government Licence http://www.nationalarchives.gov.uk/doc/non-commercial-government-licence/version/2/. ChatGPT has been used while writing some of the code for plotting the figures and Grammarly was used for language checking of parts of the manuscript.

References

Adusumilli, S., Fricker, H. A., Medley, B., Padman, L., and Siegfried, M. R.: Interannual variations in meltwater input to the Southern Ocean from Antarctic ice shelves, Nature Geoscience, 13, 616–620, https://doi.org/10.1038/s41561-020-0616-z, publisher: Nature Publishing Group, 2020.

Arakawa, A. and Lamb, V. R.: Computational Design of the Basic Dynamical Processes of the UCLA General Circulation Model, in: Methods in Computational Physics: Advances in Research and Applications, edited by Chang, J., vol. 17 of *General Circulation Models of the Atmosphere*, pp. 173–265, Elsevier, https://doi.org/10.1016/B978-0-12-460817-7.50009-4, 1977.

AVISO: AVISO Level 4 absolute dynamic topography for climate model comparison, ver.1.10.5067/DYNTO-1D1M1, 2011.

Barthélemy, A., Goosse, H., Fichefet, T., and Lecomte, O.: On the sensitivity of Antarctic sea ice model biases to atmospheric forcing uncertainties, Climate Dynamics, 51, 1585–1603, https://doi.org/10.1007/s00382-017-3972-7, 2018.

Boeira Dias, F., Rintoul, S. R., Richter, O., Galton-Fenzi, B. K., Zika, J. D., Pellichero, V., and Uotila, P.: Sensitivity of simulated water mass transformation on the Antarctic shelf to tides, topography and model resolution, Frontiers in Marine Science, 10, https://www.frontiersin.org/articles/10.3389/fmars.2023.1027704, 2023.

Bouillon, S., Fichefet, T., Legat, V., and Madec, G.: The elastic–viscous–plastic method revisited, Ocean Modelling, 71, 2–12, https://doi.org/10.1016/j.ocemod.2013.05.013, 2013.

Briegleb, B. P., Light, B., Briegleb, B. P., and Light, B.: A Delta-Eddington Multiple Scattering Parameterization for Solar Radiation, in: in the Sea Ice Component of the Community Climate System Model, Ncar Tech. Note NCAR/TN-472+STR, 2007.

Carter, G. S. and Merrifield, M. A.: Open boundary conditions for regional tidal simulations, Ocean Modelling, 18, 194–209, https://doi.org/https://doi.org/10.1016/j.ocemod.2007.04.003, 2007.

Cavalieri, D. J., Parkinson, C. L., Gloersen, P., and Zwally, H. J.: Arctic and Antarctic Sea Ice Concentrations from Multichannel Passive-Microwave Satellite Data Sets: October 1978-September 1995 User's Guide, Tech. Rep. NASA-TM-104647, NASA, https://ntrs.nasa.gov/citations/19980076134, nTRS Author Affiliations: Goddard Space Flight Center NTRS Document ID: 19980076134 NTRS Research Center: Goddard Space Flight Center (GSFC), 1997.

Chapman, D. C.: Numerical Treatment of Cross-Shelf Open Boundaries in a Barotropic Coastal Ocean Model, Journal of Physical Oceanography, 15, 1060–1075, https://doi.org/10.1175/1520-0485(1985)015<1060:NTOCSO>2.0.CO;2, aDS Bibcode: 1985JPO....15.1060C, 1985.

Charrassin, J.-B., Hindell, M., Rintoul, S. R., Roquet, F., Sokolov, S., Biuw, M., Costa, D., Boehme, L., Lovell, P., Coleman, R., Timmermann, R., Meijers, A., Meredith, M., Park, Y.-H., Bailleul, F., Goebel, M., Tremblay, Y., Bost, C.-A., McMahon, C. R., Field, I. C., Fedak, M. A., and Guinet, C.: Southern Ocean frontal structure and sea-ice formation rates revealed by elephant seals, Proceedings of the National Academy of Sciences, 105, 11 634–11 639, https://doi.org/10.1073/pnas.0800790105, publisher: Proceedings of the National Academy of Sciences, 2008.

Comiso, J. C. and Nishio, F.: Trends in the sea ice cover using enhanced and compatible AMSR-E, SSM/I, and SMMR data, Journal of Geophysical Research: Oceans, 113, https://doi.org/10.1029/2007JC004257, _eprint: https://onlinelibrary.wiley.com/doi/pdf/10.1029/2007JC004257, 2008.

Debernard, J. B., Kristersen, N. M., Maartensson, S., Wang, K., and Waagbø, G. A.: metno/metroms: Intermediate release, https://zenodo.org/records/290667, 10.5281/zenodo.290667, 2017.

Dee, D. P., Uppala, S. M., Simmons, A. J., Berrisford, P., Poli, P., Kobayashi, S., Andrae, U., Balmaseda, M. A., Balsamo, G., Bauer, P., Bechtold, P., Beljaars, A. C. M., van de Berg, L., Bidlot, J., Bormann, N., Delsol, C., Dragani, R., Fuentes, M., Geer, A. J., Haimberger, L., Healy, S. B., Hersbach, H., Hólm, E. V., Isaksen, L., Kållberg, P., Köhler, M., Matricardi, M., McNally, A. P., Monge-Sanz, B. M., Morcrette, J.-J., Park, B.-K., Peubey, C., de Rosnay, P., Tavolato, C., Thépaut, J.-N., and Vitart, F.: The ERA-Interim reanalysis: configuration and performance of the data assimilation system, Quarterly Journal of the Royal Meteorological Society, 137, 553–597, https://doi.org/10.1002/qj.828, _eprint: https://onlinelibrary.wiley.com/doi/pdf/10.1002/qj.828, 2011.

Fetterer, F., Knowles, K., Meier, W. N., Savoie, M., and Windnagel, A. K.: Sea Ice Index, Version 3, https://doi.org/https://doi.org/10.7265/N5K072F8, 2021.

Flather, R.: A tidal model of the north-west European continental shelf, https://www.semanticscholar.org/paper/A-tidal-model-of-the-north-west-European-shelf-Flather/7229fa80be4d3889aee977e70394e68076d569d1, 1976.

Gade, H. G.: Melting of Ice in Sea Water: A Primitive Model with Application to the Antarctic Ice Shelf and Icebergs, Journal of Physical Oceanography, 9, 189–198, https://doi.org/10.1175/1520-0485(1979)009<0189:MOIISW>2.0.CO;2, publisher: American Meteorological Society Section: Journal of Physical Oceanography, 1979.

Galton-Fenzi, B. K., Hunter, J. R., Coleman, R., Marsland, S. J., and Warner, R. C.: Modeling the basal melting and marine ice accretion of the Amery Ice Shelf, Journal of Geophysical Research: Oceans, 117, https://doi.org/10.1029/2012JC008214, _eprint: https://onlinelibrary.wiley.com/doi/pdf/10.1029/2012JC008214, 2012.

Gilbert, E. and Holmes, C.: 2023's Antarctic sea ice extent is the lowest on record, Weather, 79, 46–51, https://doi.org/10.1002/wea.4518, _eprint: https://onlinelibrary.wiley.com/doi/pdf/10.1002/wea.4518, 2024.

Goessling, H. F., Tietsche, S., Day, J. J., Hawkins, E., and Jung, T.: Predictability of the Arctic sea ice edge, Geophysical Research Letters, 43, 1642–1650, https://doi.org/10.1002/2015GL067232, _eprint: https://onlinelibrary.wiley.com/doi/pdf/10.1002/2015GL067232, 2016.

Good, S. A., Martin, M. J., and Rayner, N. A.: EN4: Quality controlled ocean temperature and salinity profiles and monthly objective analyses with uncertainty estimates, Journal of Geophysical Research: Oceans, 118, 6704–6716, https://doi.org/10.1002/2013JC009067, _eprint: https://onlinelibrary.wiley.com/doi/pdf/10.1002/2013JC009067, 2013.

Goosse, H., Allende Contador, S., Bitz, C. M., Blanchard-Wrigglesworth, E., Eayrs, C., Fichefet, T., Himmich, K., Huot, P.-V., Klein, F., Marchi, S., Massonnet, F., Mezzina, B., Pelletier, C., Roach, L., Vancoppenolle, M., and Van Lipzig, N. P. M.: Modulation of the seasonal cycle of the Antarctic sea ice extent by sea ice processes and feedbacks with the ocean and the atmosphere, The Cryosphere, 17, 407–425, https://doi.org/10.5194/tc-17-407-2023, 2023.

Gouretski, V. and Cheng, L.: Correction for systematic errors in the global dataset of temperature profiles from mechanical bathythermographs, Journal of Atmospheric and Oceanic Technology, 37, 841 – 855, https://doi.org/10.1175/JTECH-D-19-0205.1, place: Boston MA, USA Publisher: American Meteorological Society, 2020.

Gouretski, V. and Reseghetti, F.: On depth and temperature biases in bathythermograph data: Development of a new correction scheme based on analysis of a global ocean database, Deep Sea Research Part I: Oceanographic Research Papers, 57, 812–833, https://doi.org/10.1016/j.dsr.2010.03.011, 2010.

Haumann, F. A., Gruber, N., Münnich, M., Frenger, I., and Kern, S.: Sea-ice transport driving Southern Ocean salinity and its recent trends, Nature, 537, 89–92, https://doi.org/10.1038/nature19101, publisher: Nature Publishing Group, 2016.

Hersbach, H. and de Rosnay, P.: Operational global reanalysis: progress, future directions and synergies with NWP, https://www.ecmwf.int/en/elibrary/80922-operational-global-reanalysis-progress-future-directions-and-synergies-nwp, 2018.

Hersbach, H., Bell, B., Berrisford, P., Hirahara, S., Horányi, Muñoz-Sabater, J., Nicolas, J., Peubey, C., Radu, R., Schepers, D., Simmons, A., Soci, C., Abdalla, S., Abellan, X., Balsamo, G., Bechtold, P., Biavati, G., Bidlot, J., Bonavita, M., De Chiara, G., Dahlgren, P., Dee, D., Diamantakis, M., Dragani, R., Flemming, J., Forbes, R., Fuentes, M., Geer, A., Haimberger, L., Healy, S., Hogan, R., Hólm, E., Janisková, M., Keeley, S., Laloyaux, P., Lopez, P., Lupu, C., Radnoti, G., de Rosnay, P., Rozum, I., Vamborg, F., Villaume, S., and Thépaut, J.-N.: Complete ERA5 from 1940: Fifth generation of ECMWF atmospheric reanalyses of the global climate, https://doi.org/10.24381/cds.143582cf, 2017.

Hobbs, W., Spence, P., Meyer, A., Schroeter, S., Fraser, A. D., Reid, P., Tian, T. R., Wang, Z., Liniger, G., Doddridge, E. W., and Boyd, P. W.: Observational Evidence for a Regime Shift in Summer Antarctic Sea Ice, Journal of Climate, 37, 2263–2275, https://doi.org/10.1175/JCLI-D-23-0479.1, publisher: American Meteorological Society Section: Journal of Climate, 2024.

Holland, M. M., Bailey, D. A., Briegleb, B. P., Light, B., and Hunke, E.: Improved Sea Ice Shortwave Radiation Physics in CCSM4: The Impact of Melt Ponds and Aerosols on Arctic Sea Ice, Journal of Climate, 25, 1413–1430, https://doi.org/10.1175/JCLI-D-11-00078.1, publisher: American Meteorological Society Section: Journal of Climate, 2012.

Holland, P., Bruneau, N., Enright, C., Losch, M., Kurtz, N., and Kwok, R.: Modeled Trends in Antarctic Sea Ice Thickness, Journal of Climate, 27, 3784–3801, https://doi.org/10.1175/JCLI-D-13-00301.1, 2014.

Huneke, W. G. C., Hobbs, W. R., Klocker, A., and Naughten, K. A.: Dynamic Response to Ice Shelf Basal Meltwater Relevant to Explain Observed Sea Ice Trends Near the Antarctic Continental Shelf, Geophysical Research Letters, 50, e2023GL105 435, https://doi.org/10.1029/2023GL105435, _eprint: https://onlinelibrary.wiley.com/doi/pdf/10.1029/2023GL105435, 2023.

Hunke, E., Allard, R., Bailey, D. A., Blain, P., Craig, A., Dupont, F., DuVivier, A., Grumbine, R., Hebert, D., Holland, M., Jeffery, N., Lemieux, J.-F., Osinski, R., Rasmussen, T., Ribergaard, M., Roberts, A., and Worthen, D.: CICE-Consortium/CICE: CICE Version 6.3.1, https://doi.org/10.5281/zenodo.6314188, 2022.

Hunke, E. C. and Dukowicz, J. K.: The sea ice momentum equation in the free drift regime, Technical Report LA- UR-03-2219, Los Alamos National Laboratory, https://github.com/CICE-Consortium/CICE/blob/main/doc/PDF/LAUR-03-2219.pdf, 2003.

Hunke, E. C., Hebert, D. A., and Lecomte, O.: Level-ice melt ponds in the Los Alamos sea ice model, CICE, Ocean Modelling, 71, 26–42, https://doi.org/10.1016/j.ocemod.2012.11.008, 2013.

Hunke, E. C., Lipscomb, W. H., Turner, A. K., Jeffery, N., and Elliott, S.: CICE : The Los Alamos Sea Ice Model Documentation and Software User's Manual Version 5.1 LA-CC-06-012, https://github.com/CICE-Consortium/CICE-svn-trunk/blob/main/cicedoc/cicedoc.pdf, 2015.

Jacob, R., Larson, J., and Ong, E.: M × N Communication and Parallel Interpolation in Community Climate System Model Version 3 Using the Model Coupling Toolkit, The International Journal of High Performance Computing Applications, 19, 293–307, https://doi.org/10.1177/1094342005056116, publisher: SAGE Publications Ltd STM, 2005.

Kimura, N., Nishimura, A., Tanaka, Y., and Yamaguchi, H.: Influence of winter sea-ice motion on summer ice cover in the Arctic, Polar Research, https://doi.org/10.3402/polar.v32i0.20193, 2013.

King, J. C., Marshall, G. J., Colwell, S., Arndt, S., Allen-Sader, C., and Phillips, T.: The Performance of the ERA-Interim and ERA5 Atmospheric Reanalyses Over Weddell Sea Pack Ice, Journal of Geophysical Research: Oceans, 127, e2022JC018 805, https://doi.org/10.1029/2022JC018805, publisher: John Wiley & Sons, Ltd, 2022.

Larson, J., Jacob, R., and Ong, E.: The Model Coupling Toolkit: A New Fortran90 Toolkit for Building Multiphysics Parallel Coupled Models, The International Journal of High Performance Computing Applications, 19, 277–292, https://doi.org/10.1177/1094342005056115, publisher: SAGE Publications Ltd STM, 2005.

Lin, X., Massonnet, F., Fichefet, T., and Vancoppenolle, M.: SITool (v1.0) – a new evaluation tool for large-scale sea ice simulations: application to CMIP6 OMIP, Geoscientific Model Development, 14, 6331–6354, https://doi.org/10.5194/gmd-14-6331-2021, publisher: Copernicus GmbH, 2021.

Lipscomb, W. H. and Hunke, E. C.: Modeling Sea Ice Transport Using Incremental Remapping, Monthly Weather Review, 132, 1341–1354, https://doi.org/10.1175/1520-0493(2004)132<1341:MSITUI>2.0.CO;2, publisher: American Meteorological Society Section: Monthly Weather Review, 2004.

Lipscomb, W. H., Hunke, E. C., Maslowski, W., and Jakacki, J.: Ridging, strength, and stability in high-resolution sea ice models, Journal of Geophysical Research: Oceans, 112, https://doi.org/10.1029/2005JC003355, _eprint: https://onlinelibrary.wiley.com/doi/pdf/10.1029/2005JC003355, 2007.

Maksym, T., Stammerjohn, S. E., Ackley, S., and Massom, R.: Antarctic Sea Ice—A Polar Opposite?, Oceanography, 25, 140–151, https://doi.org/10.5670/oceanog.2012.88, 2015.

Marchesiello, P., McWilliams, J. C., and Shchepetkin, A.: Open boundary conditions for long-term integration of regional oceanic models, Ocean Modelling, 3, 1–20, https://doi.org/10.1016/S1463-5003(00)00013-5, 2001.

Martin, T. and Adcroft, A.: Parameterizing the fresh-water flux from land ice to ocean with interactive icebergs in a coupled climate model, Ocean Modelling, 34, 111–124, https://doi.org/10.1016/j.ocemod.2010.05.001, 2010.

Martinson, D. G. and McKee, D. C.: Transport of warm Upper Circumpolar Deep Water onto the western Antarctic Peninsula continental shelf, Ocean Science, 8, 433–442, https://doi.org/10.5194/os-8-433-2012, publisher: Copernicus GmbH, 2012.

Mason, E., Molemaker, J., Shchepetkin, A. F., Colas, F., McWilliams, J. C., and Sangrà, P.: Procedures for offline grid nesting in regional ocean models, Ocean Modelling, 35, 1–15, https://doi.org/https://doi.org/10.1016/j.ocemod.2010.05.007, 2010.

Meier, W., Fetterer, F., Savoie, M., Mallory, S., Duerr, R., and Stroeve, J. C.: NOAA/NSIDC Climate Data Record of Passive Microwave Sea Ice Concentration, Version 2, https://doi.org/10.7265/N55M63M1, 2013.

Meier, W. N., Fetterer, F., Windnagel, A. K., and Stewart, J. S.: NOAA/NSIDC Climate Data Record of Passive Microwave Sea Ice Concentration, Version 4, https://doi.org/https://doi.org/10.7265/efmz-2t65., 2021.

Menemenlis, D., Campin, J.-M., Heimbach, P., Hill, C., Lee, T., Nguyen, A., Schodlok, M., and Zhang, H.: ECCO2: High Resolution Global Ocean and Sea Ice Data Synthesis, Mercator Ocean Q. Newsl. 31, 13–21., 31, 2008.

Miller, U. K., Zappa, C. J., Gordon, A. L., Yoon, S.-T., Stevens, C., and Lee, W. S.: High Salinity Shelf Water production rates in Terra Nova Bay, Ross Sea from high-resolution salinity observations, Nature Communications, 15, 373, https://doi.org/10.1038/s41467-023-43880-1, publisher: Nature Publishing Group, 2024.

Nakayama, Y., Timmermann, R., Schröder, M., and Hellmer, H. H.: On the difficulty of modeling Circumpolar Deep Water intrusions onto the Amundsen Sea continental shelf, Ocean Modelling, 84, 26–34, https://doi.org/10.1016/j.ocemod.2014.09.007, 2014.

Naud, C. M., Booth, J. F., and Genio, A. D. D.: Evaluation of ERA-Interim and MERRA Cloudiness in the Southern Ocean, Journal of Climate, 27, 2109–2124, https://doi.org/10.1175/JCLI-D-13-00432.1, publisher: American Meteorological Society Section: Journal of Climate, 2014.

Naughten, K. A., Galton-Fenzi, B. K., Meissner, K. J., England, M. H., Brassington, G. B., Colberg, F., Hattermann, T., and Debernard, J. B.: Spurious sea ice formation caused by oscillatory ocean tracer advection schemes, Ocean Modelling, 116, 108–117, https://doi.org/10.1016/j.ocemod.2017.06.010, 2017.

Naughten, K. A., Meissner, K. J., Galton-Fenzi, B. K., England, M. H., Timmermann, R., Hellmer, H. H., Hattermann, T., and Debernard, J. B.: MetROMS-iceshelf, https://doi.org/10.5281/zenodo.1157230, 2018a.

Naughten, K. A., Meissner, K. J., Galton-Fenzi, B. K., England, M. H., Timmermann, R., Hellmer, H. H., Hattermann, T., and Debernard, J. B.: Intercomparison of Antarctic ice-shelf, ocean, and sea-ice interactions simulated by MetROMS-iceshelf and FESOM 1.4, Geoscientific Model Development, 11, 1257–1292, https://doi.org/10.5194/gmd-11-1257-2018, publisher: Copernicus GmbH, 2018b.

NSIDC: Antarctic sea ice extent hits a third low in a row | Arctic Sea Ice News and Analysis, https://nsidc.org/arcticseaicenews/2024/02/antarctic-sea-ice-extent-hits-third-low-in-row/, 2024.

OSI SAF: GBL SICO CDR R3Global Sea Ice Concentration Climate Data Record v3.0 - Multimission, https://doi.org/10.15770/EUM_SAF_OSI_0013, 2022.

Padman, L., Siegfried, M. R., and Fricker, H. A.: Ocean Tide Influences on the Antarctic and Greenland Ice Sheets, Reviews of Geophysics, 56, 142–184, https://doi.org/10.1002/2016RG000546, _eprint: https://onlinelibrary.wiley.com/doi/pdf/10.1002/2016RG000546, 2018.

Parkinson, C. L.: A 40-y record reveals gradual Antarctic sea ice increases followed by decreases at rates far exceeding the rates seen in the Arctic, Proceedings of the National Academy of Sciences, 116, 14 414–14 423, https://doi.org/10.1073/pnas.1906556116, publisher: Proceedings of the National Academy of Sciences, 2019.

Purich, A. and Doddridge, E. W.: Record low Antarctic sea ice coverage indicates a new sea ice state, Communications Earth & Environment, 4, 1–9, https://doi.org/10.1038/s43247-023-00961-9, publisher: Nature Publishing Group, 2023.

Rintoul, S., van Wijk, E., Wahlin, A., and Boehme, L.: Seeing below the ice: a strategy for observing the ocean beneath antarctic sea ice and ice shelves, Tech. rep., Southern Ocean Observing System, 2014.

Rintoul, S. R.: The global influence of localized dynamics in the Southern Ocean, Nature, 558, 209–218, https://doi.org/10.1038/s41586-018-0182-3, 2018.

Roach, L. A., Dörr, J., Holmes, C. R., Massonnet, F., Blockley, E. W., Notz, D., Rackow, T., Raphael, M. N., O'Farrell, S. P., Bailey, D. A., and Bitz, C. M.: Antarctic Sea Ice Area in CMIP6, Geophysical Research Letters, 47, e2019GL086 729, https://doi.org/10.1029/2019GL086729, _eprint: https://onlinelibrary.wiley.com/doi/pdf/10.1029/2019GL086729, 2020.

Rothrock, D. A.: The energetics of the plastic deformation of pack ice by ridging, Journal of Geophysical Research (1896-1977), 80, 4514–4519, https://doi.org/10.1029/JC080i033p04514, _eprint: https://onlinelibrary.wiley.com/doi/pdf/10.1029/JC080i033p04514, 1975.

Sallée, J.-b., Wienders, N., Speer, K., and Morrow, R.: Formation of Subantarctic Mode Water in the southeastern Indian Ocean, Ocean Dynamics, 56, 525–542, https://doi.org/10.1007/s10236-005-0054-x, 2006.

Sallée, J.-B., Shuckburgh, E., Bruneau, N., Meijers, A. J. S., Bracegirdle, T. J., and Wang, Z.: Assessment of Southern Ocean mixed-layer depths in CMIP5 models: Historical bias and forcing response, Journal of Geophysical Research: Oceans, 118, 1845–1862, https://doi.org/10.1002/jgrc.20157, _eprint: https://onlinelibrary.wiley.com/doi/pdf/10.1002/jgrc.20157, 2013.

Sallée, J.-B., Pellichero, V., Akhoudas, C., Pauthenet, E., Vignes, L., Schmidtko, S., Garabato, A. N., Sutherland, P., and Kuusela, M.: Fifty-year changes of the world ocean's surface layer in response to climate change, https://doi.org/10.5281/zenodo.5776180, 2021a.

Sallée, J.-B., Pellichero, V., Akhoudas, C., Pauthenet, E., Vignes, L., Schmidtko, S., Garabato, A. N., Sutherland, P., and Kuusela, M.: Summertime increases in upper-ocean stratification and mixed-layer depth, Nature, 591, 592–598, https://doi.org/10.1038/s41586-021-03303-x, publisher: Nature Publishing Group, 2021b.

Schmidtko, S., Heywood, K. J., Thompson, A. F., and Aoki, S.: Multidecadal warming of Antarctic waters, Science (New York, N.Y.), 346, 1227–1231, https://doi.org/10.1126/science.1256117, 2014.

Schroeter, S. and Sandery, P. A.: Large-ensemble analysis of Antarctic sea ice model sensitivity to parameter uncertainty, Ocean Modelling, 177, 102 090, https://doi.org/10.1016/j.ocemod.2022.102090, 2022.

https://doi.org/10.5194/gmd-2024-213
Preprint. Discussion started: 13 December 2024

Screen, J. A.: Sudden increase in Antarctic sea ice: Fact or artifact?, Geophysical Research Letters, 38, https://doi.org/10.1029/2011GL047553, _eprint: https://onlinelibrary.wiley.com/doi/pdf/10.1029/2011GL047553, 2011.

Shchepetkin, A. F. and McWilliams, J. C.: The regional oceanic modeling system (ROMS): a split-explicit, free-surface, topography-following-coordinate oceanic model, Ocean Modelling, 9, 347–404, https://doi.org/10.1016/j.ocemod.2004.08.002, 2005.

Timmermann, R., Le Brocq, A., Deen, T., Domack, E., Dutrieux, P., Galton-Fenzi, B., Hellmer, H., Humbert, A., Jansen, D., Jenkins, A., Lambrecht, A., Makinson, K., Niederjasper, F., Nitsche, F., Nøst, O. A., Smedsrud, L. H., and Smith, W. H. F.: A consistent data set of Antarctic ice sheet topography, cavity geometry, and global bathymetry, Earth System Science Data, 2, 261–273, https://doi.org/10.5194/essd-2-261-2010, publisher: Copernicus GmbH, 2010.

Tschudi, M. A., Meier, W. N., Stewart, J. S., Fowler, C., and Maslanik, J.: Polar Pathfinder Daily 25 km EASE-Grid Sea Ice Motion Vectors, Version 4, https://nsidc.org/data/nsidc-0116/versions/4, 2019.

Turner, A. K., Hunke, E. C., and Bitz, C. M.: Two modes of sea-ice gravity drainage: A parameterization for large-scale modeling, Journal of Geophysical Research: Oceans, 118, 2279–2294, https://doi.org/10.1002/jgrc.20171, _eprint: https://onlinelibrary.wiley.com/doi/pdf/10.1002/jgrc.20171, 2013.

Uotila, P., Goosse, H., Haines, K., Chevallier, M., Barthélemy, A., Bricaud, C., Carton, J., Fučkar, N., Garric, G., Iovino, D., Kauker, F., Korhonen, M., Lien, V. S., Marnela, M., Massonnet, F., Mignac, D., Peterson, K. A., Sadikni, R., Shi, L., Tietsche, S., Toyoda, T., Xie, J., and Zhang, Z.: An assessment of ten ocean reanalyses in the polar regions, Climate Dynamics, 52, 1613–1650, https://doi.org/10.1007/s00382-018-4242-z, 2019.

Wang, H., Klekociuk, A. R., French, W. J. R., Alexander, S. P., and Warner, T. A.: Measurements of Cloud Radiative Effect across the Southern Ocean (43° S–79° S, 63° E–158° W), Atmosphere, 11, 949, https://doi.org/10.3390/atmos11090949, number: 9 Publisher: Multidisciplinary Digital Publishing Institute, 2020a.

Wang, H., Zhang, L., Chu, M., and Hu, S.: Advantages of the latest Los Alamos Sea-Ice Model (CICE): evaluation of the simulated spatiotemporal variation of Arctic sea ice, Atmospheric and Oceanic Science Letters, 13, 1–8, https://doi.org/10.1080/16742834.2020.1712186, 2020b.

Worby, A. P. A. P. ., Geiger, C. A., Paget, M. J., Van Woert, M. L., Ackley, S. F., and DeLiberty, T. L.: Thickness distribution of Antarctic sea ice, http://udspace.udel.edu/handle/19716/16748, publisher: American Geophysical Union, 2008.

Wu, H., Xu, X., Luo, T., Yang, Y., Xiong, Z., and Wang, Y.: Variation and comparison of cloud cover in MODIS and four reanalysis datasets of ERA-interim, ERA5, MERRA-2 and NCEP, Atmospheric Research, 281, 106 477, https://doi.org/10.1016/j.atmosres.2022.106477, 2023.

Wunsch, C., Heimbach, P., Ponte, R., and Fukumori, I.: The Global General Circulation of the Ocean Estimated by the ECCO-Consortium, Oceanography, 22, 88–103, https://doi.org/10.5670/oceanog.2009.41, 2009.

Xu, Y., Li, H., Liu, B., Xie, H., and Ozsoy-Cicek, B.: Deriving Antarctic Sea-Ice Thickness From Satellite Altimetry and Estimating Consistency for NASA's ICESat/ICESat-2 Missions, Geophysical Research Letters, 48, e2021GL093 425, https://doi.org/10.1029/2021GL093425, _eprint: https://onlinelibrary.wiley.com/doi/pdf/10.1029/2021GL093425, 2021.

Zhang, J.: Modeling the Impact of Wind Intensification on Antarctic Sea Ice Volume, Journal of Climate, 27, 202–214, https://doi.org/10.1175/JCLI-D-12-00139.1, publisher: American Meteorological Society Section: Journal of Climate, 2014.

Zwally, H. J., Comiso, J. C., Parkinson, C. L., Campbell, W. J., Carsey, F. D., and Gloersen, P.: Antartic sea ice, 1973 - 1976: Satellite passive-microwave observations, Tech. rep., https://ntrs.nasa.gov/citations/19840002650, number: NASA-SP-459, 1983.

Zweng, M. M., Reagan, J. R., Antonov, J. I., Locarnini, R. A., Mishonov, A. V., Boyer, T. P., Garcia, H. E., Baranova, O. K., Johnson, D. R., Seidov, D., and Biddle, M. M.: World ocean atlas 2013. Volume 2, Salinity, https://doi.org/10.7289/V5251G4D, publisher: U.S. Department of Commerce, National Oceanic and Atmospheric Administration, National Environmental Satellite, Data and Information Service, 2013.

Äijälä, C. and Nie, Y.: MetROMS evaluation scripts, https://doi.org/10.5281/zenodo.14186139, 2024.

Äijälä, C. and Uotila, P.: MetROMS-UHel, https://doi.org/10.5281/zenodo.14185734, 2024.